



The Origin and Evolution of Ly α Blobs in Cosmological Galaxy Formation Simulations

Benjamin Kimock¹, Desika Narayanan^{1,2,3}, Aaron Smith^{4,17}, Xiangcheng Ma^{5,6}, Robert Feldmann⁷, Daniel Anglés-Alcázar^{8,9}, Volker Bromm¹⁰, Romeel Davé^{11,12,13}, James E. Geach¹⁴, Philip Hopkins¹⁵, and Dušan Kereš¹⁶

¹ Department of Astronomy, University of Florida, 211 Bryant Space Sciences Center, Gainesville, FL 32611, USA

² University of Florida Informatics Institute, 432 Newell Drive, CISE Bldg E251, Gainesville, FL 32611, USA

³ Cosmic Dawn Center at the Niels Bohr Institute, University of Copenhagen and DTU-Space, Technical University of Denmark, Denmark

⁴ Department of Physics, Massachusetts Institute of Technology, Cambridge, MA 02139, USA

⁵ Department of Astronomy and Theoretical Astrophysics Center, University of California Berkeley, Berkeley, CA 94720, USA

⁶ TAPIR, MC 350-17, California Institute of Technology, Pasadena, CA 91125, USA

⁷ Institute for Computational Science, University of Zurich, Zurich CH-8057, Switzerland

⁸ Center for Computational Astrophysics, Flatiron Institute, 162 Fifth Avenue, New York, NY 10010, USA

⁹ Department of Physics, University of Connecticut, 196 Auditorium Road, U-3046, Storrs, CT 06269-3046, USA

¹⁰ Department of Astronomy, The University of Texas at Austin, Austin, TX 78712, USA

¹¹ Institute for Astronomy, Royal Observatory, University of Edinburgh, Edinburgh EH9 3HJ, UK

¹² University of the Western Cape, Bellville, Cape Town 7535, South Africa

¹³ South African Astronomical Observatories, Observatory, Cape Town 7925, South Africa

¹⁴ Centre for Astrophysics Research, School of Physics, Astronomy and Mathematics, University of Hertfordshire, College Lane, Hatfield AL10 9AB, UK

¹⁵ TAPIR, Mailcode 350-17, California Institute of Technology, Pasadena, CA 91125, USA

¹⁶ Department of Physics, Center for Astrophysics and Space Science, University of California at San Diego, 9500 Gilman Drive, La Jolla, CA 92093, USA

Received 2020 April 17; revised 2020 September 29; accepted 2020 October 4; published 2021 March 10

Abstract

High-redshift Ly α blobs (LABs) are an enigmatic class of objects that have been the subject of numerous observational and theoretical investigations. It is of particular interest to determine the dominant power sources for their luminosity, as direct emission from H II regions, cooling gas, and fluorescence due to the presence of active galactic nuclei (AGNs) can all contribute significantly. In this paper, we present the first theoretical model to consider all of these physical processes in an attempt to develop a model for the origin of LABs. This is achieved by combining a series of high-resolution cosmological zoom-in simulations with ionization and Ly α radiative transfer models. We find that massive galaxies display a range of Ly α luminosities and spatial extents (which strongly depend on the limiting surface brightness used) over the course of their lives, though regularly exhibit luminosities and sizes consistent with observed LABs. The model LABs are typically powered from a combination of recombination in star-forming galaxies, as well as cooling emission from gas associated with accretion. When AGNs are included in the model, the fluorescence caused by active galactic nucleus-driven ionization can be a significant contributor to the total Ly α luminosity as well. Within our modeled mass range, there are no obvious threshold physical properties that predict the appearance of LABs, and only weak correlations of the luminosity with the physical properties of the host galaxy. This is because the emergent Ly α luminosity from a system is a complex function of the gas temperature, ionization state, and Ly α escape fraction.

Unified Astronomy Thesaurus concepts: [Galaxies \(573\)](#); [Galaxy formation \(595\)](#); [Radiative transfer simulations \(1967\)](#)

1. Introduction

Ly α “blobs” (LABs) are an enigmatic class of objects first discovered roughly two decades ago (Fynbo et al. 1999; Steidel et al. 2000), and are characterized by their copious Lyman α (Ly α) luminosities and large spatial extent. While there is no consensus for the definition of an LAB, the majority of blobs have luminosities in excess of $\sim 10^{43}$ erg s⁻¹, and spatial extents that are greater than ~ 50 kpc in radius. We will discuss these definitions in more detail shortly.

Since their discovery, the dominant source of power in these objects has been under debate. Broadly, there are two major sources: (i) in situ emission from H II regions surrounding actively star-forming regions in the central galaxy or satellites (e.g., Geach et al. 2016) that is subsequently scattered in the circumgalactic gas, and (ii) direct radiation from extended gas in the halo. Emission from the latter can be due to either cooling radiation from a collisionally excited circumgalactic

medium (e.g., Katz et al. 1996; Haiman et al. 2000; Fardal et al. 2001; Trebitsch et al. 2016; Mandelker et al. 2020), or photoionized gas originating from the meta-galactic UV background (UVB) and starbursts or active galactic nuclei (AGNs) driving Ly α production via H II recombination (Kollmeier et al. 2010; Gronke & Bird 2017).

Claims of LABs powered by cooling accretion from the intergalactic medium (IGM) are often observationally justified by the detection of LABs without any observable AGNs. For example, Smith & Jarvis (2007) observed a blob at $z = 2.83$ for which they were able to rule out AGNs based on non-detections of highly ionized lines. Similarly, Smith & Jarvis (2007) ruled out direct emission from H II regions based on a relatively low derived star formation rate (SFR) from the UV continuum of $\sim 25 M_{\odot}$ yr⁻¹. Scarlata et al. (2009) identified an LAB that is associated with two galaxies, and present spectroscopic evidence against emission driven by star formation or AGNs, as they do not detect C IV or N V lines. Nilsson et al. (2006) also argued against the presence of AGNs

¹⁷ NHFP Einstein Fellow.

Table 1
An Overview of Ly α Properties for a Sample of Known LABs That We Compare Our Simulations to

| Publication | z | $L_{\text{Ly}\alpha}$ (10^{43} erg s $^{-1}$) | Σ_{lim} (10^{-18} erg s $^{-1}$ cm $^{-2}$ arcsec $^{-2}$) | Area (arcsec 2) |
|------------------------|---------|--|---|------------------------|
| Matsuda et al. (2004) | 3.1 | 0.9–11.0 | 2.2 | 16–222 |
| Nilsson et al. (2006) | 3.16 | 1.0 | 3.7 | 47 |
| Smith & Jarvis (2007) | 2.83 | 21.0 | ... | 110 |
| Ouchi et al. (2009) | 6.595 | 3.9 | 1.63 | 7 |
| Yang et al. (2009) | 2.3 | 1.6–5.3 | 2.47 | 25 |
| Matsuda et al. (2011) | 3.09 | 0.8–20.4 | 1.4 | 28–181 |
| Steidel et al. (2011) | 2.65 | 6.57 | ~ 1 | 30 |
| Barger et al. (2012) | 0.977 | 0.72 | ... | 500 |
| Prescott et al. (2013) | 1.7–2.7 | 0.26–1.9 | 0.933 | 5.9–104 |
| Caminha et al. (2016) | 3.118 | 0.19 | ... | 14 |
| Bădescu et al. (2017) | 2.3 | 0.9–1.3 | 2.1 | 10–12 |
| North et al. (2017) | 3.08 | 2.2 | 7.5 | 7–12 |
| Shibuya et al. (2018) | 5.7–6.6 | 1.26–7.94 | 10.0–21.0 | 2–3 |

or superwinds based on the lack of a continuum counterpart detection in a $z = 3.16$ blob (though this is debated, see, e.g., Prescott et al. 2015). Other recent studies have supported arguments of a lack of AGNs with measurements of the kinematics of circumgalactic gas in order to argue for gas accretion as the dominant power source (e.g., Daddi et al. 2020; Herenz et al. 2020). At the same time, other authors have argued against gravitational cooling dominating the power source owing to a lack of kinematic inflow signatures (e.g., Yang et al. 2011, 2014).

At the same time, other studies argue heavily for active galactic nucleus (AGN)-driven fluorescence.¹⁸ For example, some LABs are radio loud (Miley & De Breuck 2008), with correlated Ly α and radio extents. This correlation implies that a central AGN may be powering the extended Ly α (van Ojik et al. 1997). Indeed, the heavily studied LAB 1 appears to be powered by a hidden quasar (Overzier et al. 2013), based on observations of [O III], and it is argued that AGNs may power the most luminous LABs. Kim et al. (2020) utilized polarization mapping of a $z \sim 2.5$ LAB to suggest powering by an AGN. Geach et al. (2009) report X-ray observations of LABs, finding an AGN fraction of $17_{-7}^{+12}\%$, but with all (5 of 29) detections they find heavy obscuration and suggest that there may be heavily obscured AGNs in many LABs.

The tendency of LABs to appear in over-dense environments (Prescott et al. 2008; Matsuda et al. 2009, 2011) suggests that the power source may relate to elevated SFRs typically associated with the formation of massive galaxies (e.g., Matsuda et al. 2007; Kubo et al. 2013; Alexander et al. 2016; Hine et al. 2016). However, care should be taken in assessing the role of star formation in powering LABs, since the signatures of elevated star formation and AGN activity can be nearly identical (Webb et al. 2009).

LABs may also be powered indirectly by AGNs or star formation through galaxy-scale winds (Wilman et al. 2005). Based on detections of bubbles in LAB 1 (Steidel et al. 2000), Matsuda et al. (2004) deduced an SFR of $\sim 600 M_{\odot} \text{yr}^{-1}$, which is in agreement with submillimeter observations (Chapman et al. 2001). Matsuda et al. (2007) also argued for the possibility of extended starbursts or winds on the basis of correlated submillimeter and Ly α emission in LAB 1.

Additionally, Ohyama et al. (2003) interpreted the double-peaked Ly α spectrum, particularly the decrease in the velocity separation of the two peaks with the distance from the center of LAB 1 as evidence of wind-driven Ly α .

The last two decades of observations have brought little consensus on the dominant source(s) of emission in LABs, or even whether a single physical process dominates. Indeed, some authors think that LABs may be powered by a variety of mechanisms (Nilsson et al. 2006; Prescott et al. 2009; Scarlata et al. 2009; Webb et al. 2009; Ao et al. 2015). There is increasing acknowledgement of the kinematic complexities of these objects (Herenz et al. 2020), and recent evidence that the presence of infalling gas does not necessarily predict that cooling dominates Ly α emission (Ao et al. 2020; Smith 2020). Additionally, the physics of Ly α escape from high-redshift galaxies remains an open problem in connection with LABs, though it is deeply coupled to the emission thereof (Smith et al. 2019). This leaves these massive objects largely unexplained in spite of their relevance to massive galaxy formation and reionization, as we do not understand what if anything the Ly α traces.

1.1. Definition of a Ly α blob

There is no consensus on the definition of an LAB in the literature. We present in Table 1 a summary of recent papers aimed at observationally characterizing LABs, and quote their measurements of a few observed properties that could potentially be used to distinguish this class of objects from Ly α emitters (LAEs). As is evident, there is no clear luminosity threshold for an LAB definition. Observations find luminosities ranging nearly two orders of magnitude (2×10^{42} erg s $^{-1} < L_{\text{Ly}\alpha} < 2.1 \times 10^{44}$ erg s $^{-1}$). Similarly, there is no clear size definition. Quoted diameters range from 30–200 kpc, though the interpretation of this physical constraint is muddled by the fact that observations have a wide range of surface brightness sensitivities that range by over an order of magnitude in the literature. Beyond this, the dispersion in this limiting surface brightness along with the amorphous morphology of LABs makes such size measurements difficult to interpret. To further complicate matters, recent work by Wisotzki et al. (2018) has shown that with sufficient sensitivity nearly the whole sky is covered by Ly α . Indeed, as we will demonstrate in this work, the area enclosed by an LAB is a strong function of the limiting surface brightness.

¹⁸ Fluorescence is the same physical effect as recombination. Typically, in the literature, recombination is referred to as fluorescence in regions associated with recent star formation.

Going forward in this paper, we will adopt a notional threshold luminosity for a blob definition of $L_{\text{Ly}\alpha} > 10^{43}$ erg s⁻¹, with no size threshold. This said, we will explore the impact of modifying this on our results.

1.2. Theoretical Efforts to Date

Furlanetto et al. (2005), Laursen & Sommer-Larsen (2007), Cen & Zheng (2013), Geach et al. (2016), and Gronke & Bird (2017) have studied the contribution of star formation on the formation of LABs, and all concluded this source of Ly α can (or in the case of Cen & Zheng 2013 *must*) have power blobs. Additionally, Cen & Zheng (2013) were able to reproduce an observed LAB luminosity–size relation. However, some of the previous work on the contribution of star formation relies on a simplified SFR– $L_{\text{Ly}\alpha}$ conversion based on the expected luminosity from case B recombination.

There has also been extensive study of the contribution of Ly α emission due to collisionally excited neutral hydrogen (Haiman et al. 2000; Fardal et al. 2001; Faucher-Giguère et al. 2010; Goerdt et al. 2010; Rosdahl & Blaizot 2012; Trebitsch et al. 2016; Mandelker et al. 2020), or specifically the incoming streams of cooling IGM that are observed in some simulations at high redshift. These works are able to reproduce the requisite Ly α luminosity to power an LAB, but sometimes have difficulty with the particular appearance of LABs in surface brightness maps.

Other authors have studied the effect of fluorescence from an external ionizing field such as a nearby or internal quasar (Haiman & Rees 2001) or the cosmological UV background or winds (Furlanetto et al. 2005; Mas-Ribas & Dijkstra 2016). These authors found that an external ionizing radiation field can produce extended Ly α emission, but not quite at the surface brightnesses to produce a blob on its own.

Missing, to date, is a comprehensive model that considers all of these physical processes simultaneously. In this paper, we attempt to provide just that. We present a model for the formation and evolution of LABs by combining high-resolution cosmological zoom-in simulations with ionization radiative transfer and Ly α radiative transfer. We consider the physics of emission from ionized gas surrounding massive stars, cooling, and fluorescence induced from an external ionizing field (including AGNs). In Section 2, we detail our numerical methodology. In Section 3, we describe the evolution of the Ly α luminosity from massive galaxies at high redshift. We follow this in Section 4 with an investigation into the dominant power sources of Ly α photons in massive galaxies. We investigate the role of an AGN in Section 5, and discuss the broader physical properties of our model LABs in Section 6. We provide discussion in Section 7 and conclude in Section 8.

2. Methods

2.1. Overview

Our overall goal is to extract Ly α observables from cosmological zoom-in simulations of massive galaxies in evolution in post-processing. To do this, we construct a pipeline in which we smooth the particle data onto an octree grid on which we perform ionizing radiative transfer, to determine the ionization state of the gas in the halo. We then perform Ly α radiative transfer calculations in order to compute both the intrinsic Ly α luminosity (considering both

Table 2
Physical Properties for the Simulations We Use at $z = 5$, within Our (150 kpc)³ Box

| Name | M_{DM} (M_{\odot}) | $R_{\text{vir}}^{\text{a}}$ (kpc) | M_{star} (M_{\odot}) | SFR ($M_{\odot} \text{ yr}^{-1}$) |
|------|------------------------------------|--------------------------------------|--------------------------------------|--|
| A1 | 9.72×10^{11} | 5.60×10^1 | 2.07×10^{10} | 3.11×10^1 |
| A2 | 3.98×10^{11} | 4.20×10^1 | 3.81×10^9 | 2.65×10^1 |
| A4 | 2.98×10^{11} | 3.81×10^1 | 1.32×10^9 | 4.70×10^0 |
| A8 | 3.04×10^{11} | 3.84×10^1 | 9.38×10^8 | 8.18×10^0 |

Note.

^a Calculated using Bryan & Norman (1997).

Table 3
Physical Properties for the Simulations We Use at $z = 2$, within Our (150 kpc)³ Box

| Name | M_{DM} (M_{\odot}) | $R_{\text{vir}}^{\text{a}}$ (kpc) | M_{star} (M_{\odot}) | SFR ($M_{\odot} \text{ yr}^{-1}$) |
|------|------------------------------------|--------------------------------------|--------------------------------------|--|
| A1 | 1.64×10^{12} | 1.20×10^2 | 1.78×10^{11} | 6.55×10^1 |
| A2 | 2.00×10^{12} | 1.29×10^2 | 2.98×10^{11} | 1.68×10^2 |
| A4 | 1.63×10^{12} | 1.19×10^2 | 1.41×10^{11} | 7.15×10^1 |
| A8 | 1.92×10^{12} | 1.26×10^2 | 8.06×10^{10} | 8.79×10^1 |

Note.

^a Calculated using Bryan & Norman (1997).

recombination and collisional processes), as well as the escape fraction from the region. In what follows, we go into substantially more detail about each of these numerical techniques. The reader who is less interested in our numerical implementation may skip the remainder of this section without loss of continuity, though we encourage them to peruse Tables 2 and 3 for an overview of the physical properties of our model galaxies.

2.2. Cosmological Hydrodynamic Zoom Galaxy Formation Simulations

The galaxy formation simulations studied here were presented in Anglés-Alcázar et al. (2017b), which are part of the Feedback In Realistic Environments (FIRE) project.¹⁹ These simulations employ the FIRE-2 suite of physics (Hopkins et al. 2018), and their initial conditions are derived from the MassiveFIRE suite (Feldmann et al. 2016). These physics modules are fully described in Hopkins et al. (2018), and we point the reader to this work, summarizing the salient details.

The initial conditions for the MassiveFIRE simulations are generated with MUSIC (Hahn & Abel 2011) for a $(100 \text{ cMpc}/h)^3$ box.²⁰ We first run an initial low-resolution simulation, from which we selected particular halos for re-simulation at much higher resolution. For these halos, the region encompassing the high-resolution particles was selected with a convex hull filter selecting all particles within 3 virial radii of the halo at $z = 1$. These particles were then split to obtain higher mass resolution, and the entire simulation was rerun with a final mass resolution of the high-resolution particles of $m_{\text{DM}} = 1.7 \times 10^5 M_{\odot}$ and $m_{\text{baryon}} = 3.3 \times 10^4 M_{\odot}$ for dark matter and baryons, respectively.

¹⁹ See the FIRE project website at <http://fire.northwestern.edu>.

²⁰ This is the only instance in this paper where we mention comoving units, all other scales quoted are in physical units.

The simulations themselves are run with GIZMO (Hopkins 2015) with the hydrodynamics run in the meshless finite mass mode. These simulations include star formation in dense and self-gravitating gas (Hopkins et al. 2013), and stellar feedback channels that include radiation pressure, photoionization, photoelectric heating, O-star and asymptotic giant branch (AGB) driven stellar winds, and Type I and II supernovae. Supermassive black holes are included in the simulations, but followed passively, meaning that feedback from AGNs is not included. That said, black holes accreted following the torque-limited accretion model of Anglés-Alcázar et al. (2017a, 2017b). In this paper, we examine four massive halos, whose physical properties are described at $z = 2$ and $z = 5$ in Tables 2 and 3, respectively. These halos have the same initial conditions as those monikered “A1,” “A2,” “A4,” and “A8” from Feldmann et al. (2016), though are different from the original halos in that they are run with FIRE-2 physics (the original halos presented in Feldmann et al. are run with FIRE-1 physics (Hopkins et al. 2014) and did not include super massive black holes). See Cochrane et al. (2019) and Wellons et al. (2020) for detailed studies of the spatially resolved dust continuum emission in the central galaxies of these halos as well as their kinematic and structural properties.

2.3. Computing the Ionization State of the Gas

The first post-processing step in the cosmological galaxy formation simulations is to compute the ionization state of the gas. To do this, we employ LYCRT (Ma et al. 2015, 2020).

LYCRT is a Monte Carlo radiative transfer code that iteratively computes the gas ionization state by emitting rays from both stars and a UV background. The radiative transfer is performed on an octree grid, containing the smoothed information from the particle data. These rays are subject to absorption by H I along with dust scattering and absorption, using a constant dust-to-metal ratio of 0.4 below 10^6 K, no dust above 10^6 K, and the SMC grain size from Weingartner & Draine (2001). The passage of these rays through octree cells is used to compute the ionizing UV field.

The ionization state of the gas is updated based on the UV field after each iteration, and includes collisions with electrons when solving for the thermal state (Fumagalli et al. 2011).²¹ We assume a redshift-dependent UV background with intensity as determined by the model of Faucher-Giguère et al. (2009). The stellar spectral energy distributions (SEDs) are generated with Binary Population and Spectral Synthesis (BPASS) spectral libraries that include the effect of binary stars (Eldridge et al. 2008).

Later in this work we will use this ionization state calculation to add an approximate model for the effects of an AGN, wherein we effectively treat the AGN as a very bright star particle. A complete description of how we derive the ionizing intensity for each AGN is included in Section 5, along with a discussion of their effects.

²¹ Since our ionization solver does not update the gas temperature the ionization state is self-inconsistent: the gas surrounding massive stars may be underheated. However, this inaccuracy likely induces only a small change to the total Ly α emissivity as the recombination coefficient varies weakly with temperature.

2.4. Ly α Emission and Radiative Transfer

The Ly α Monte Carlo radiative transfer calculations are performed using the Cosmic Ly α transfer Code (COLT; Smith et al. 2015). COLT models the emission of Ly α photons due to hydrogen recombination and radiative de-excitation of collisionally excited hydrogen, and accounts for scattering due to neutral hydrogen, and scattering and absorption due to dust.

To do this, COLT generates Monte Carlo photon packets in octree cells with probability proportional to the Ly α luminosity of each cell. We provide a more detailed discussion of the recombination and collisional emission processes in Section 4.1.²² Photons are sampled uniformly over the unit sphere, and the sub-grid positions are randomly distributed within cell volumes. The transport of photon packets follows the usual Monte Carlo scheme, with the local Ly α absorption coefficient given by

$$k_\alpha = n_{\text{H I}} \sigma_\alpha(\nu), \quad (1)$$

where $\sigma_\alpha(\nu)$ is the Ly α cross section, which at line center is $5.9 \times 10^{-14} [T/(10^4 \text{ K})]^{-1/2} \text{ cm}^2$. Following Laursen et al. (2009), we assume SMC-like dust properties with an effective cross section per hydrogen atom of $3.95 \times 10^{-22} \text{ cm}^2$, and fiducial albedo of 0.32. We do not alter the mechanisms for scattering, but do make an adjustment to how dust absorption is accounted for. Instead of drawing a random variable to determine if a photon packet is absorbed by an interaction with dust (as done by Laursen & Sommer-Larsen 2007 and Smith et al. 2015) we treat dust absorption as a continuous process. Each photon packet has a weight that is attenuated at each scattering by the amount of dust it traversed since its last scattering. Therefore, we can compute the escape fraction from the simulation as the sum of the weights of all photon packets upon escaping the simulation.

Beyond the standard COLT algorithms, we have developed a number of performance-enhancing features. For example, to avoid following extremely low weight photon paths we introduce a conservative traversed optical depth threshold, after which we discard photons from the simulation. We verified that each algorithmic change does not alter the final luminosity or surface brightness of our model galaxies. Similarly, we have introduced updated communication modules into COLT that distribute photon packets individually with asynchronous message passing interface communication patterns, as opposed to batches of photons. We find this allows for a nearly 30% speedup due to the large variance in computation time per photon packet within photon batches, i.e., this minimizes the time individual nodes sit idle.

3. Ly α Histories of Massive Halos

3.1. Evolution of Massive Galaxies

To help orient the reader, in Figure 1, we first plot the evolution of one of our model simulations, halo A4. We pick this model as we will use it throughout the paper as a fiducial

²² In addition to the underheating issues described in Footnote 19, the FIRE simulations include only a crude treatment of self-shielding in the gas, which can drive temperatures in the *opposite* direction, i.e., toward overheating. This can impact the emergent Ly α luminosity substantially due to the strong dependence of the collisional rate coefficients on temperature (e.g., Faucher-Giguère et al. 2010). In Appendix A, we investigate the impact of these temperature inaccuracies in detail.

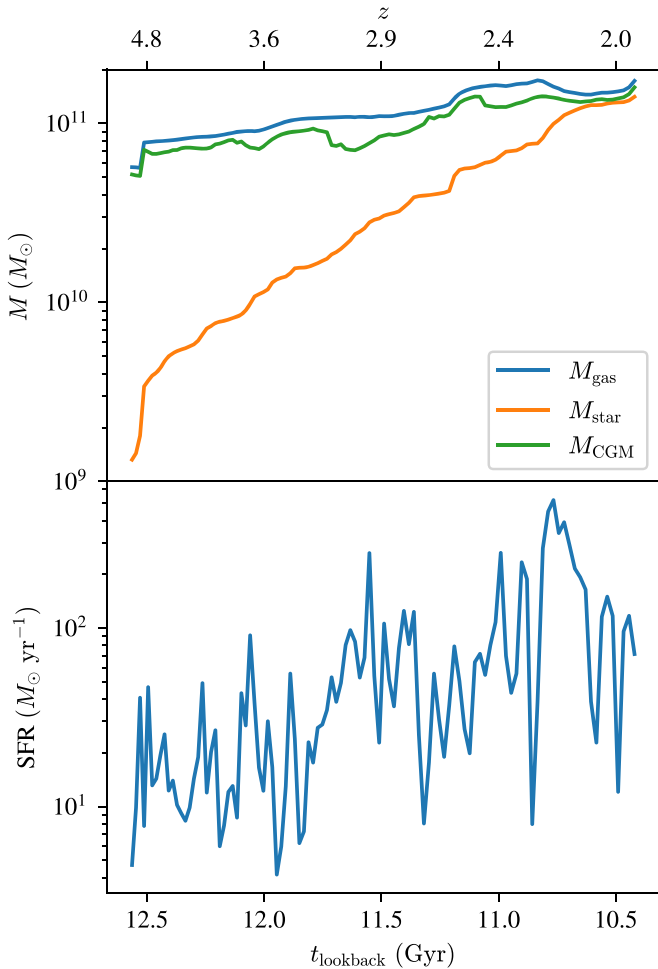


Figure 1. Evolution of physical properties for a sample halo (A4). We show (from top to bottom) the total gas mass, stellar mass, SFR, and circumgalactic medium (CGM) gas, defined as all gas in the box not associated with the central galaxy. The physical properties are computed over the $(150 \text{ kpc})^3$ box employed for our radiative transfer calculations.

galaxy to examine, though note that the results presented in this paper are generic to all of our model halos. The physical properties presented in Figure 1 are not of the central galaxy or halo, but rather the $(150 \text{ kpc})^3$ box over which we will perform our radiative transfer simulations.

Figure 2 shows 75 kpc postage stamps of our fiducial model halo at integer redshifts between $z = 2-5$. We show the total $\text{Ly}\alpha$ luminosity, $\text{Ly}\alpha$ surface brightness, gas surface brightness, and stellar surface densities. We will return to Figure 2 repeatedly throughout this paper, though note that large $\text{Ly}\alpha$ luminosities and extended morphologies are evident at a range of times in the galaxy’s history.

3.2. Formation of LABs

The first question we pursue is whether our simulations can actually form an LAB. Recalling Section 1.1, there is no formal definition of what constitutes an LAB. We therefore explore two reasonable criteria for objects classified as LABs in comparison to our simulations.

We first consider a total $\text{Ly}\alpha$ luminosity-based definition. When we quote the luminosity of a simulated blob we mean the total luminosity of the simulation domain; we do not use a simulated aperture. In Figure 3, we plot the $\text{Ly}\alpha$ luminosity for

our model galaxies as a function of time from $z \approx 2-6$. For comparison, we also show the $\text{Ly}\alpha$ luminosities for a number of observed LABs mentioned in Table 1. The $\text{Ly}\alpha$ luminosity of our model galaxies varies substantially, but broadly overlap with the observed range of luminosities over the considered redshift range.

At the same time, LABs are known not only for their prodigious $\text{Ly}\alpha$ luminosity, but also their extended morphologies. Some studies therefore employ surface brightness profiles to characterize the spatial extent of objects (e.g., Wisotzki et al. 2018). However, as we will demonstrate, the blob morphologies are sufficiently disordered and asymmetric that it is not entirely obvious how to define a radial profile. In order to characterize blobs by their surface brightness, in Figure 4, we plot the area enclosed by a number of isophotes as a function of the isophotal luminosity. We also attempt to compare these to known LABs (from Table 1). Since we want to plot an area and most publications only mention a radius or semimajor axis of a blob, we assume such observed blobs are circular to deduce an area, and therefore denote these as upper limits since the true beam filling factor is likely lower than unity. This comparison to LABs is preferable to a surface brightness profile because while both collapse the azimuthal dimension to assist in easy comparison between objects, a surface brightness profile typically assumes azimuthal symmetry, which is typically not the case for LABs.

As is evident from Figures 3 and 4, our model galaxies display reasonable $\text{Ly}\alpha$ luminosities and enclosed areas as a function of limiting surface brightness when compared to observations. In Figure 5, we take a $z \sim 2$ snapshot of our fiducial model and convolve the model $\text{Ly}\alpha$ surface brightness with the point source function (PSF) of the Multi Unit Spectroscopic Explorer (MUSE) at the Very Large Telescope. We note that the observed morphology when convolved with observed PSFs resembles the observations.

We have presented a luminosity-based definition and an area-based definition, but these properties are correlated, so our model LABs should occupy a similar region in area-luminosity space. Our ability to compare with literature is limited, because we must select a surface brightness cutoff and a PSF with which to compute an area, but in the literature each study has their own cutoff and PSF. In Figure 6 we present a comparison of our model with the LAB (candidates) presented in Matsuda et al. (2004, 2011) because those papers report a large number of objects and have similar PSF and luminosity threshold used to compute an area. Overall our match is decent; the one notable deviation is that our model does not match the areas for the brightest observed blobs (which is hinted at by Figure 4), and that our AGN model has relatively little impact on the maximal area (we will discuss this result later in Section 5).

We now spend most of the remainder of this paper unpacking Figures 3 and 4, exploring *why* these galaxies emit copious $\text{Ly}\alpha$ emission.

4. Origins of Observed $\text{Ly}\alpha$ Photons in Giant Blobs

In this section, we conduct a series of numerical experiments in order to characterize the driving sources of $\text{Ly}\alpha$ radiation from our model blobs. We investigate the relative contributions of emission from gas cooling and recombinations (Figures 7 and 8), the impact of the ionizing UV background (Figure 9), and the presence of an AGN (Figure 10). We find that our model LABs can be powered by a combination of

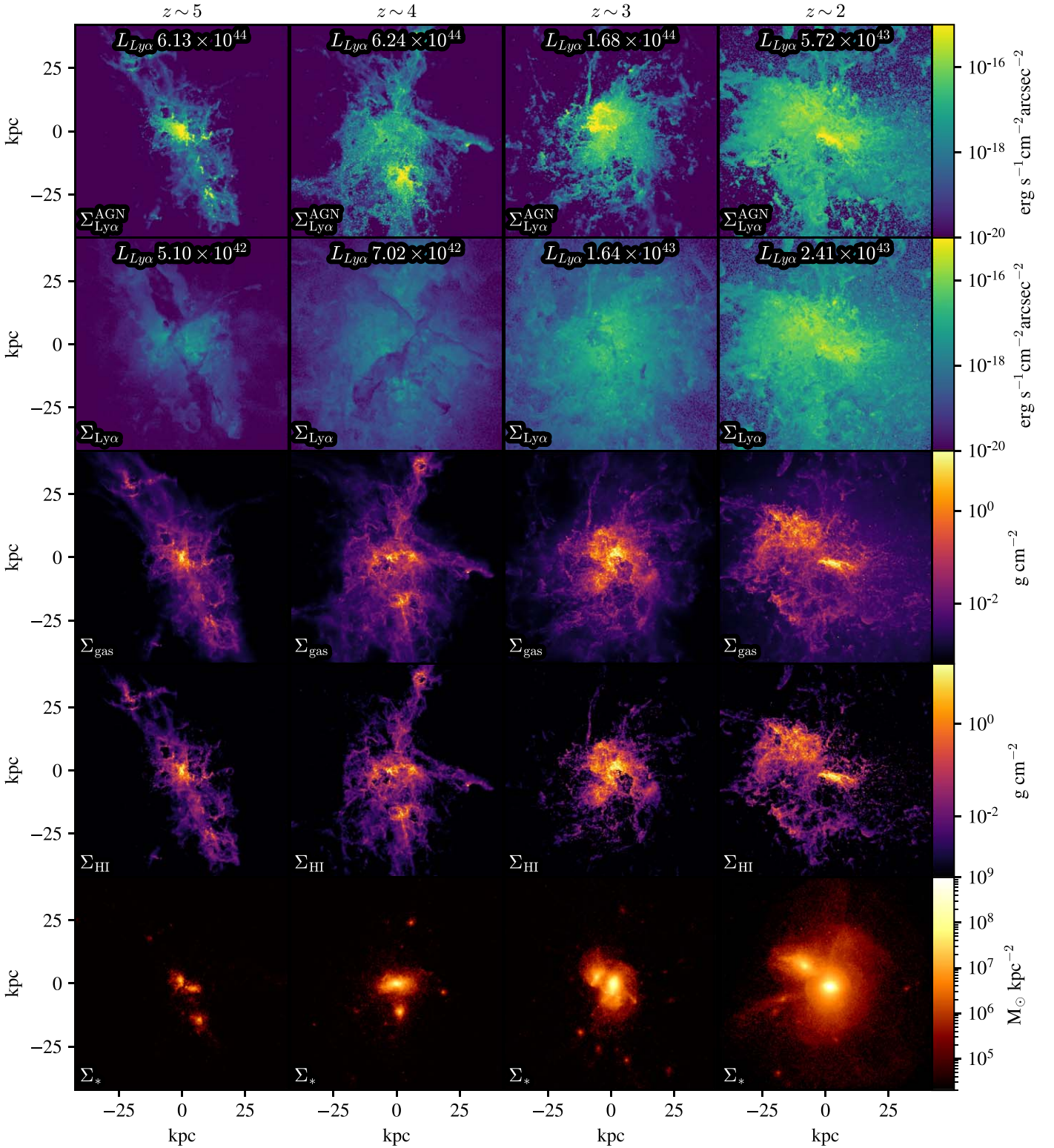


Figure 2. Ly α surface brightness with our AGN model (top row), Ly α surface brightness without our AGN model (second row), gas surface density (third row), neutral hydrogen gas surface density (fourth row), and stellar surface density (bottom row) at four redshifts for galaxy A4. All images are 75×75 physical kpc across, corresponding to $11.7''$, $10.5''$, $9.5''$, and $8.7''$ across, respectively. Each row shares the same color scale. Though our Ly α radiative transfer (RT) code produces spectra, we defer the analysis of these to another paper.

recombination in star-forming galaxies, as well as cooling from accretion, which we define as emission from collisionally excited neutral hydrogen. When we include a model for the influence of an AGN, this also contributes significantly to the

LAB luminosities. As we will show, the relative contribution to the total Ly α power from each emission source varies strongly over cosmic time, reflecting the diverse physical conditions that occur during massive galaxy evolution.

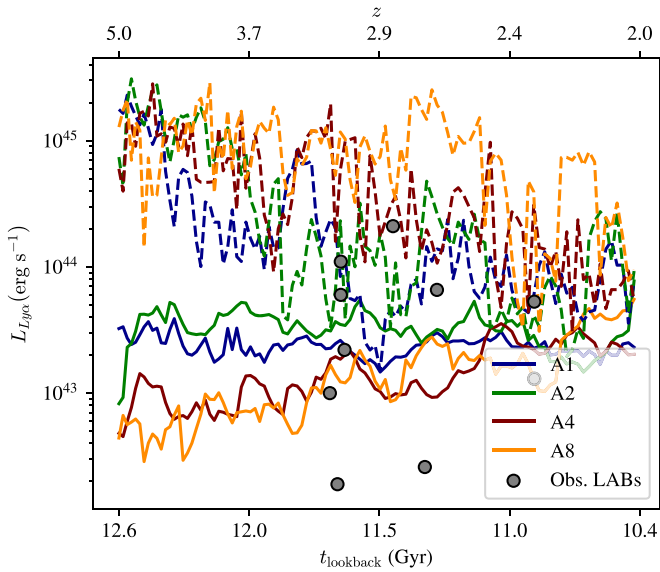


Figure 3. Ly α luminosity (median over all sightlines) for each galaxy in our sample without (solid lines) and with (dashed lines) an AGN, alongside observational data from Table 1 overplotted as gray points. Broadly, our LABs fall within the range of observed objects between $z = 5$ and $z = 2$.

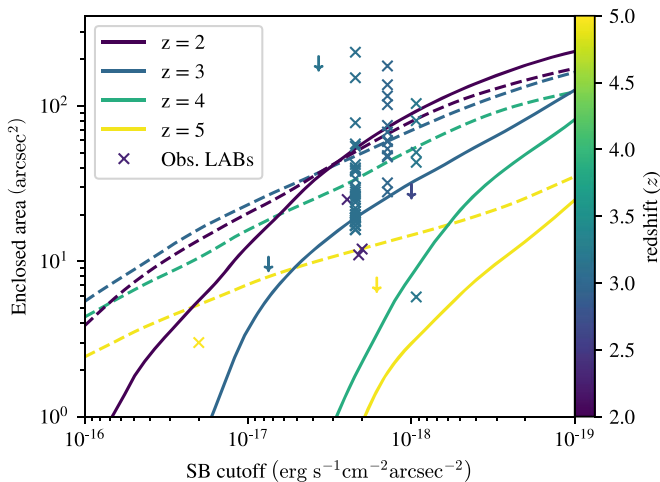


Figure 4. Comparison of blob sizes in our models to literature sizes. We define the size as the area enclosed with in a surface brightness contour after convolving with a $0.6''$ PSF, and plot models that both include an AGN (dashed lines) as well as those that do not (solid lines). Though this plot is made in square arcseconds as opposed to physical kpc, angular size varies by less than a factor of 2 over the redshift range we study ($2 < z < 5$), which is not substantial on these axes.

4.1. Basic Physical Concepts

We first discuss the basic physics driving Ly α emission from cooling gas and emission from ionized hydrogen recombining in a parcel of gas before applying these insights to our model galaxies. The physics controlling emission from these two sources is coupled; consequently, we discuss emission from cooling gas and recombinations simultaneously.

Cooling emission is primarily driven by gas accretion onto the central galaxy, and produces Ly α emission by collisionally exciting neutral hydrogen with free electrons. The rate of cooling emission is therefore proportional to the product of

neutral hydrogen and free electron densities:

$$L_{\text{Ly}\alpha}^{\text{col}} = h\nu_{\alpha} \int C_{1s2p}(T) n_e n_{\text{H I}} dV, \quad (2)$$

where $C_{1s2p}(T)$ is the temperature-dependent collisional rate coefficient (Scholz & Walters 1991), and has units of $\text{cm}^3 \text{s}^{-1}$. $h\nu_{\alpha}$ denotes the energy of a Ly α photon, n_e the number density of electrons, and $n_{\text{H I}}$ the number density of neutral hydrogen. Since we mostly deal with environments that have high ionization fractions, the free electron number density is approximately equal to the number density of ionized hydrogen, and thus the collisional excitation is maximized where approximately half the hydrogen is ionized.

While emission from collisional excitation is driven by the presence of H I and free electrons, star formation produces Ly α by case B recombination in heavily ionized regions. These recombinations emit Ly α at a rate which is proportional to $n_e n_{\text{H II}}$, given by

$$L_{\text{Ly}\alpha}^{\text{rec}} = h\nu_{\alpha} \int P_{\text{B}}(T) \alpha_{\text{B}}(T) n_e n_{\text{H II}} dV, \quad (3)$$

where $P_{\text{B}}(T)$ is the Ly α conversion probability per recombination event and $\alpha_{\text{B}}(T)$ is the case B recombination coefficient (Hui & Gnedin 1997; Cantalupo et al. 2005; Dijkstra 2014).

To demonstrate the relationship between the sources of Ly α emission and gas physical conditions, in Figure 11, we set up a controlled idealized experiment in which we bathe a 1 cm^3 cube of gas at the mean density ($7.22 \times 10^{-24} \text{ g cm}^{-3}$) in our simulations in a radiation field with intensity J_{UV} (in a flat spectrum between 13.6 and 24.6 eV), and plot two limiting cases for the luminosity of this specific volume of gas as a function of temperature: with low $J_{\text{UV}}^{\text{min}} = 0 \text{ erg cm}^{-2} \text{ s}^{-1} \text{ sr}^{-1} \text{ Hz}^{-1}$ and high $J_{\text{UV}}^{\text{max}} = 10^{-5} \text{ erg cm}^{-2} \text{ s}^{-1} \text{ sr}^{-1} \text{ Hz}^{-1}$. The high-UV value was chosen to fully ionize the gas.²³

We first consider the $J_{\text{UV}}^{\text{min}}$ case in Figure 11 (purple). Here, emission is maximized near $T = 10^4 \text{ K}$, because the impact of the gas temperature on collisionally driven Ly α emission is twofold. In the very low temperature regime, the ionization rate is sufficiently low that there are no free electrons to collisionally excite the gas. As the ionized fraction increases with temperature, there are more free electrons but less neutral hydrogen to be collisionally excited. However the second effect of temperature is to increase the rate of collisions, which produces a strong mitigating effect against the dropping abundance of neutral hydrogen; even as the gas approaches being fully ionized at high temperatures the rate of collisions mitigates the drop in luminosity.

Turning now to the $J_{\text{UV}}^{\text{max}}$ case in our idealized numerical experiment (top panel of Figure 11, orange lines) the Ly α emission from recombination declines slowly with temperature. The $J_{\text{UV}}^{\text{max}}$ also has a different temperature dependence. The gas is maximally ionized at all temperatures, but we see a decline in emissivity with temperature because the cross section of the electrons and hydrogen nuclei drop as their thermal velocities

²³ Note that in Figure 11 we plot the Ly α luminosity across the full temperature range seen in our simulations, but the analytical approximation we use for $P_{\text{B}}(T)$ only extends out to 10^5 K because that is the limit of the tables in Pengelly (1964). Therefore, we have shaded this region of the plot to indicate that this region where $P_{\text{B}}(T)$ is being extrapolated from the analytic formulation. It is likely these tables do not extend to very high temperatures because hydrogen will be mostly collisionally ionized (depending on the density).

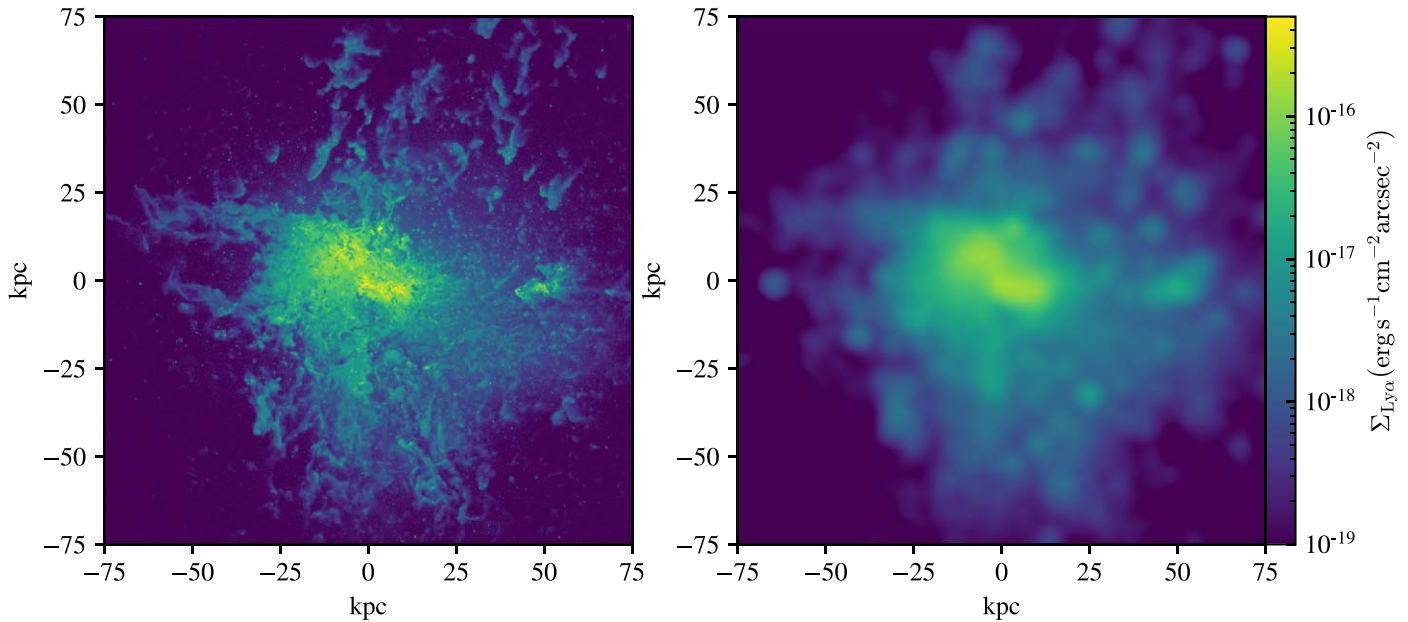


Figure 5. In the left panel we show one of our surface brightness images at a very high resolution, and in the right panel we convolve the surface brightness down to the $0.6''$ resolution at $z = 2$ (2.5 kpc) of MUSE with Gaussian noise at $\sigma = 10^{-18} \text{ erg s}^{-1} \text{ cm}^{-2} \text{ arcsec}^{-2}$ to produce an image that more closely resembles current observations of LABs.

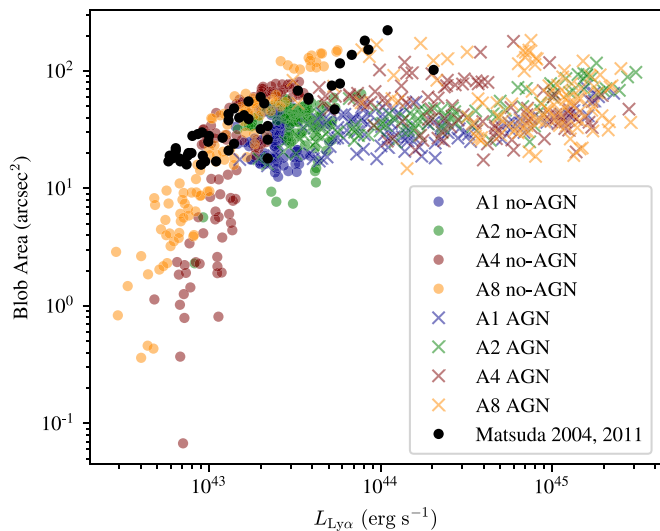


Figure 6. Comparison of our blobs vs. those published in Matsuda et al. (2004, 2011) in luminosity-area space, with and without our AGN model. We convolve to the 1.0 arcsec^2 PSF used in these publications and compute the area at $1.4 \times 10^{-18} \text{ erg s}^{-1} \text{ cm}^{-2} \text{ arcsec}^{-2}$, the same as in Matsuda et al. (2011). The areas in Matsuda et al. (2004) are computed at a threshold of $2.2 \times 10^{-18} \text{ erg s}^{-1} \text{ cm}^{-2} \text{ arcsec}^{-2}$.

increase, making recombination less likely. Note that in this experiment, where the the UV field should completely ionize the hydrogen, it is prevented from doing so to preserve numerical stability: the neutral fraction is restricted from dropping below 10^{-10} . As a result, in this extreme scenario, the collisional emissivity is driven by this neutral fraction floor, and is therefore unphysical. Accordingly, we do not plot the collisional emissivity in the $J_{\text{UV}}^{\text{max}}$ case in Figure 11. The luminosity due to collisional excitations which is produced by this numerical artifact is many orders of magnitude below the

luminosity due to recombinations. Removing it would not alter the results presented in this work.

The trends in our controlled experiment (Figure 11) provide us with the physical insight we need to understand which gas in our simulation is emitting Ly α and which gas is not. In the bottom panel of Figure 11, we show the cumulative distribution of recombination and collisionally excited emission in a single snapshot. From this we can see that the bulk of the Ly α photons are produced by “cold” photoionized gas ($T < 5 \times 10^3 \text{ K}$) and the “warm” collisionally excited gas ($6 \times 10^3 \text{ K} \leq T \leq 10^4 \text{ K}$). The emission sources (recombination and collisional de-excitation) are segregated by temperature on account of the astrophysical mechanisms responsible for the gas temperature. Cooler, recombining gas typically lies at high densities with efficient cooling and must be ionized primarily by a nearby UV source, i.e., newly formed stars.

4.2. Ly α Emission from Cosmological Simulations of Massive Galaxy Evolution

Now that we have built insight into the physics of Ly α emission from collisional excitation and recombination in an idealized experiment, we turn to our galaxy evolution simulations to understand the dominant sources of Ly α luminosity in our model LABs.

In Figure 7 we plot independently the recombination and collisional excitation components of our fiducial LAB’s luminosity. The contributions from recombination and collisions vary dramatically over the course of the model halo’s evolution, though by and large emission from collisionally excited hydrogen dominates, and grows over redshift as this galaxy grows. Integrating over our redshift of interest ($2 \leq z \leq 5$) we find $\frac{\int L_{\text{Ly}\alpha}^{\text{col}} dt}{\int (L_{\text{Ly}\alpha}^{\text{col}} + L_{\text{Ly}\alpha}^{\text{rec}}) dt} = 0.80$. In Section 5 we will discuss the impact of including an AGN in these models;

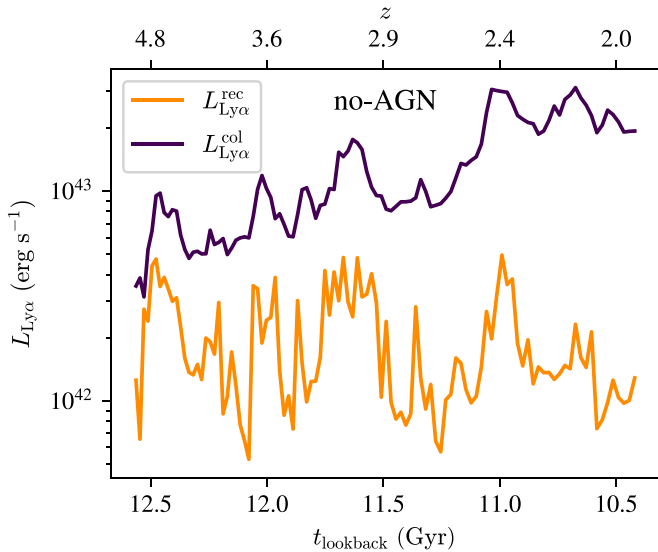


Figure 7. $\text{Ly}\alpha$ luminosity from our fiducial LAB broken down by source of emission as a function of redshift. Without an AGN the collisional excitation (purple curve) dominates over the recombination emission (orange curve).

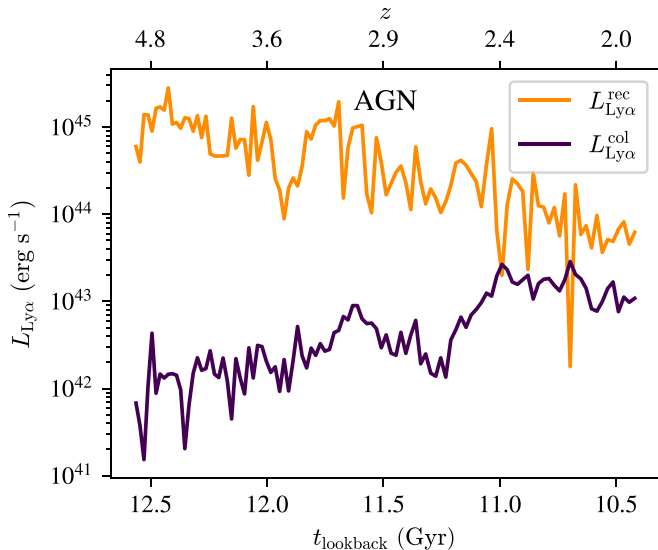


Figure 8. Galaxy A4 emission broken down by source of emission over redshift; as opposed to Figure 7 this plot includes the effect of an AGN. In the presence of an AGN the collisional excitation remains qualitatively the same, but the recombination emission becomes dominant. Both stellar and AGN sources result in large recombination luminosity fluctuations but with longer and shorter duty cycles, respectively.

when we include AGN emission from recombinations dominates and the above ratio becomes 0.03.

It is tempting to ask whether the dominant power source (i.e., recombinations versus collisions) are correlated with an obvious physical property of the galaxy? Across our three galaxies, we do not discover any strong trends (plots of this nonresult can be found in Appendix B). The reason for this is complex: as we demonstrated in Figure 11, the relative contribution of recombinations and collisions is a complex function of both the gas temperature and incident radiation field on a given parcel of gas. Galaxies have a large distribution of temperatures and ionization states that vary over the course of their lifetimes, and this distribution does not vary smoothly

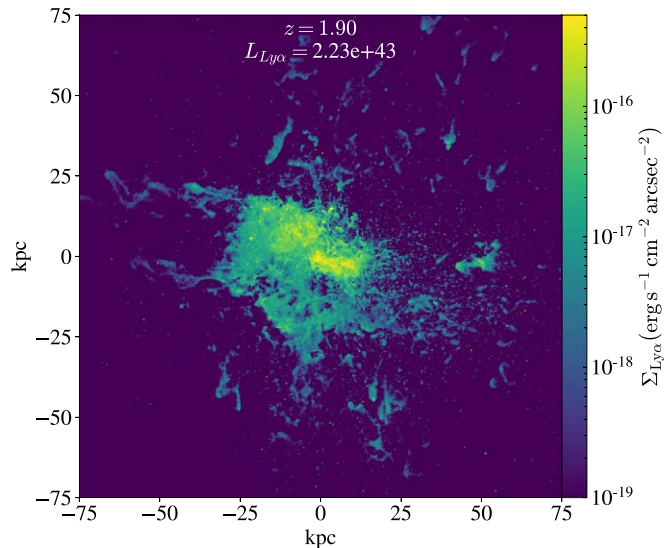


Figure 9. The morphology of a $\text{Ly}\alpha$ blob is eroded by using a stronger UV background. The primary effect of additional ionization due to background is to cause the light emitted by star formation activity to escape faster compared to Figure 5, which uses the Faucher-Giguère et al. (2009) UV background.

with a single physical property. The radiation fields are dependent on the small-scale clumping and opacity variations across the galaxy, which result in the dominant power source (recombinations versus collisions) varying non-monotonically across the galaxy. We can see this explicitly in Figure 12, where we show the morphology of galaxy A4 at redshift $z = 3$ while isolating the recombination driven and collisionally driven luminosity, respectively. The former naturally peaks at the center of the galaxy, where AGN and star formation-driven ionization peaks. However, emission from both physical processes is significant across the bulk of the main disk.

5. Impact of an AGN on $\text{Ly}\alpha$ Emission from Massive Halos

We now turn our attention to the influence of an AGN on our modeled $\text{Ly}\alpha$ emission. We note that we do not explicitly include AGN feedback; instead, from the perspective of the hydrodynamic simulations, black holes are included as passive sink particles that only accrete (Section 2). That said, we are able to assess their impact on the emission properties of the simulations in postprocessing. Here, we treat the AGN as an ionizing source when we compute the ionization state of the gas with LYCRT. In this model, the AGN SED is modeled by employing the Hopkins et al. (2007) templates for unreddened quasars, with the luminosity being tied only to the mass of the black hole particle (as opposed to the accretion rate in the simulation) by assuming the black hole is always accreting at the Eddington rate, with an efficiency of $\eta = 0.1$.²⁴ In what follows, we investigate the impact of an AGN on the total $\text{Ly}\alpha$ luminosity, as well as the overall spatial extent of the blob.

5.1. Impact of an AGN on the Luminosity and Escape Fraction

In Figure 10, we plot a comparison of the time evolution of the $\text{Ly}\alpha$ luminosity, $\text{Ly}\alpha$ escape fraction, and ionized gas

²⁴ It should be noted that this is an overly simplistic model of an AGN, neglecting departures from isotropic radiation, accretion rate variability, and the impact of radiative and mechanical feedback on the thermodynamic state of the gas.

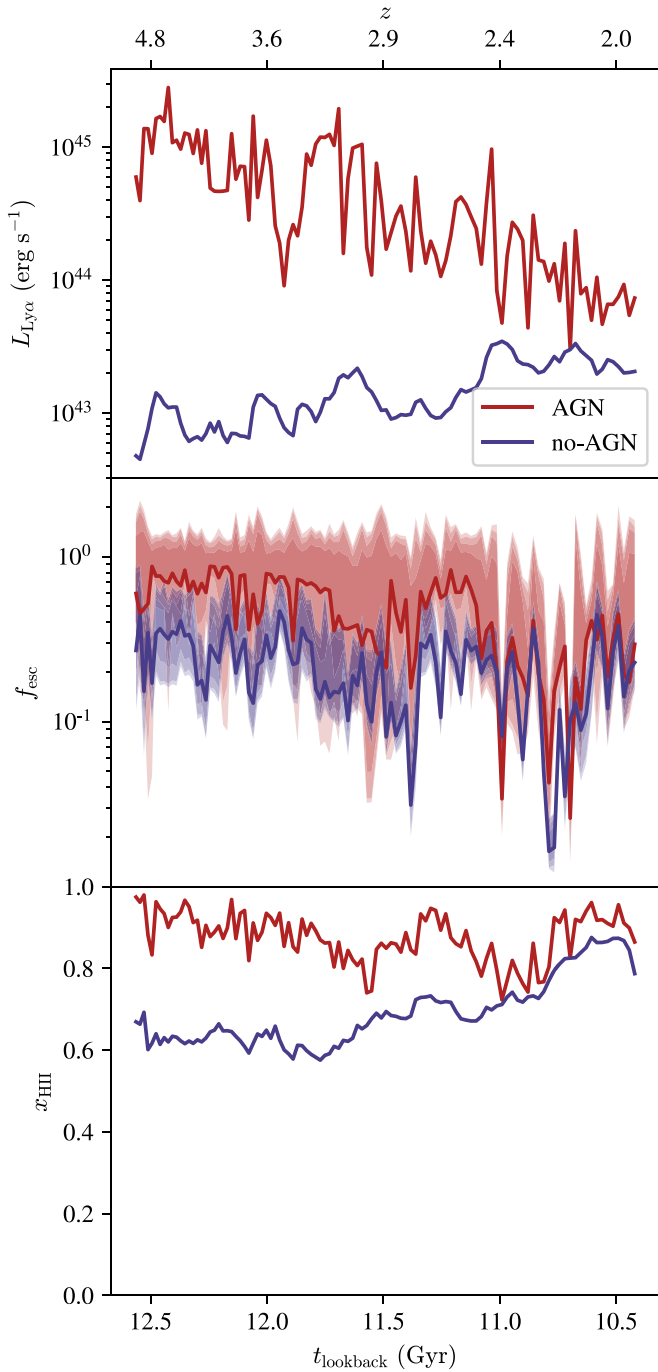


Figure 10. We compare the Ly α luminosity, Ly α escape fraction, and ionization state of the galaxy and halo with and without an AGN model. In the escape fraction plot the shaded regions represent 1σ , 2σ , and 3σ . The luminosity of an LAB can be substantially enhanced by the AGN model. The simulation domain is always heavily ionized, but the presence of an AGN also provides stochastic enhancements, though it does not well correlate with luminosity or escape fraction.

fraction for models with and without an AGN for our fiducial galaxy. As is evident, there are significant differences in a model that includes an AGN compared to one that does not.²⁵

²⁵ The snapshots this work is based on are not sufficiently high resolution to capture some small-scale clumping in the multiphase ISM, and therefore we may be overestimating the ionization of the gas in general but specifically in the presence of an AGN due to a lack of small self-shielded clumps.

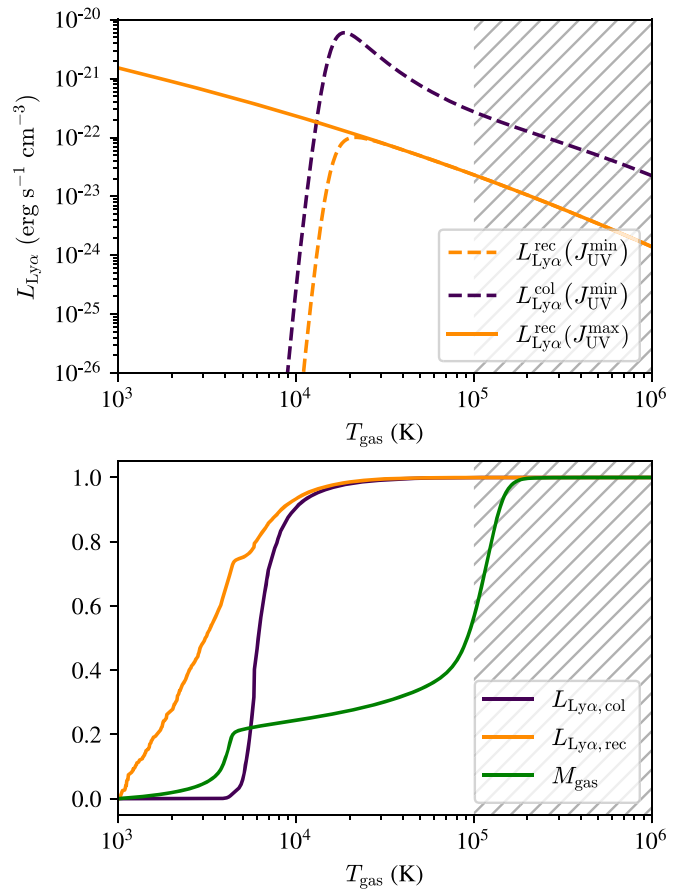


Figure 11. In the top panel, we show the Ly α luminosity for a parcel of gas at the mean density and metallicity in our simulations as a function of temperature. The dashed lines represent the luminosity of the fiducial gas at a minimal UV field, and the solid line at the maximal UV field. In both panels, the purple curves represent Ly α emission due to collisionally excited neutral hydrogen, and the orange curves represent emission due to hydrogen recombination. The gray-hatched region for $T > 10^5$ K indicates a temperature range for which we have extrapolated the Ly α conversion probability per recombination event as these probabilities are not computed at $T > 10^5$ K in the Pengelly (1964) tables that we utilize. In the bottom panel, we show the cumulative distribution of escaping Ly α by source, with respect to the temperature of the gas it is emitted from. In our simulations, we find that the Ly α emission from recombination traces a cooler population of gas than the emission due to collisional excitations. But we also observe that there is a substantial quantity of gas which does not emit strongly at all (because it is too hot or diffuse) and which does not participate in Ly α scattering (because it is fully ionized by its elevated temperature).

Since Ly α escape is sightline dependent we show in the second panel of Figure 10 the variation of our fiducial LAB's escape fraction (and therefore luminosity) over sightlines, with ionization due to an AGN and without. The observed luminosity can vary substantially due to the viewing angle of the galaxy when AGNs are present. To demonstrate this explicitly, in Figure 13, we plot the 3σ relative variation between sightlines to show how different a single physical object may appear to an observer who can only view the object from one line of sight. We use 3σ as a way to quantify the range of possible observed values, but since we only use 3072 lines of sight to compute the related percentiles, the 3σ values are sensitive to only ~ 10 lines of sight. Therefore, we include the 1σ quantities as well because though they do not have quite the same meaning, they closely resemble the 3σ quantities, which indicates the darker 3σ curves are not extremely sensitive to outliers. This huge variation when AGNs are

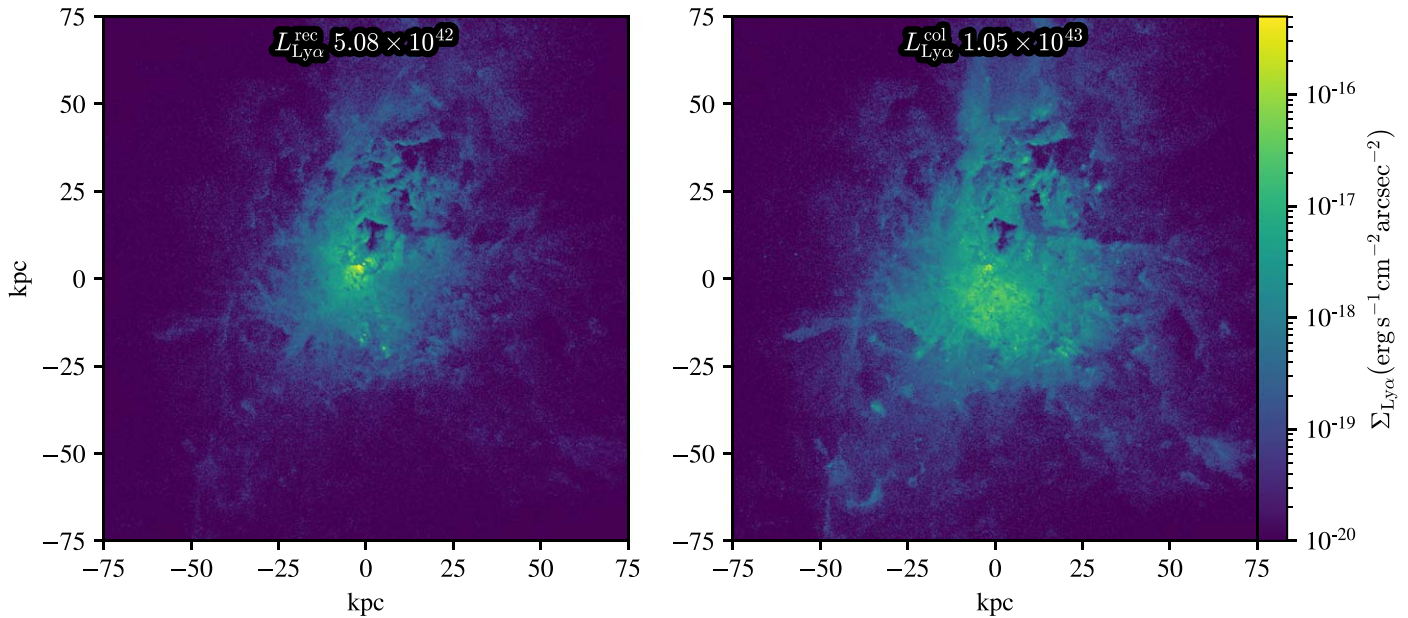


Figure 12. The $z = 3.0$ snapshot from galaxy A4 with only emission from recombinations, in the left panel, and only emission from collisional excitation on the right panel. Note that the emission from recombination and emission from collisional excitation is distributed differently across the halo.

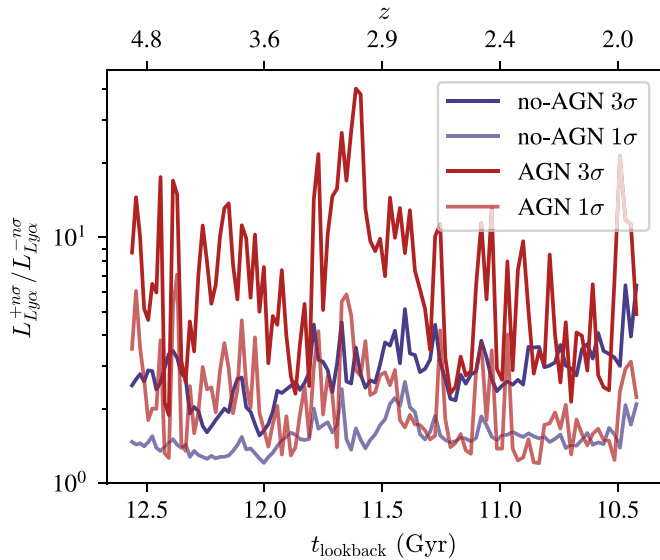


Figure 13. Maximum fractional difference in luminosity (or escape fraction) between lines of sight over redshift for one of our halos that forms an LAB, with and without an AGN. The value on the y-axis is notionally by what factor the luminosity of the object varies with respect to different lines of sight.

present is caused by the distinct nonuniformity of CGM opacity; the AGN is able to punch large ionization holes in the enclosing CGM through which $\text{Ly}\alpha$ readily escapes. It is important to note that the distribution of escape fractions is not normal; we sample 3072 sightlines to produce the middle panel of Figure 10, which is sufficient to explore many of the high-escape pathways out of an LAB. Because of this sightline variation, an escape fraction (or luminosity) calculated along a single line of sight may not be particularly representative of the overall galaxy properties. However, individual sightlines are still meaningful to probe the representative statistics of observed galaxy populations, especially because the observed distributions are a convolution of the sightline-independent distributions with sightline dependence of observables.

When we include a model for an AGN (which drives increased ionization in the gas), there are substantial spikes in the luminosity owing to increased emission from recombinations. In short, the primary effects are to increase the total $\text{Ly}\alpha$ luminosity due to the increased ionization fraction of the gas. Recall from Section 4.1 that as we increase the ionization state of the gas at a fixed temperature, e.g., $T \sim 10^4$ K, the luminosity from recombinations increases while that from collisional excitations decreases. Additionally, the escape fraction increases with the addition of an AGN (middle panel of Figure 10), due to the fact that the $\text{Ly}\alpha$ scattering strength depends primarily on $n_{\text{H I}}$ (Equation (1)). This escape fraction enhancement is so substantial that some orientations exhibit $f_{\text{esc}} > 1$ due to particular geometries that cause more $\text{Ly}\alpha$ photons to scatter into the line of sight than are absorbed.

Taken together, the increase in the ionization state of the gas (bottom panel of Figure 10) increases both the emission from recombinations, as well as the escape fraction of $\text{Ly}\alpha$ photons. These combined effects allow for significant boosting (\sim factors of 10–50) of the $\text{Ly}\alpha$ luminosity compared to a no-AGN model.

5.2. Impact of an AGN on the Spatial Extent and Concentration of $\text{Ly}\alpha$ in Blobs

As in the overall $\text{Ly}\alpha$ luminosity, the AGN can also affect the spatial extent of $\text{Ly}\alpha$ emission in massive halos. This takes two forms: (i) the total area enclosed within a surface brightness contour and (ii) the concentration of $\text{Ly}\alpha$ light in the system. We explore these in turn.

Previously, in Figure 4, we examined the size of our model LABs as a function of observation sensitivity (solid lines) in a fiducial model that did not have an AGN on. We now turn to the dashed lines in the same figure where we have included the AGN.

We see an enhancement of blob size at high surface brightness cutoffs, which indicates that there are regions that have been substantially enhanced in brightness, but at the same time we see a decrease in blob size at much lower cutoffs. We interpret this effect as a complex interaction of the gas ionization state with escape pathways. As gas becomes more

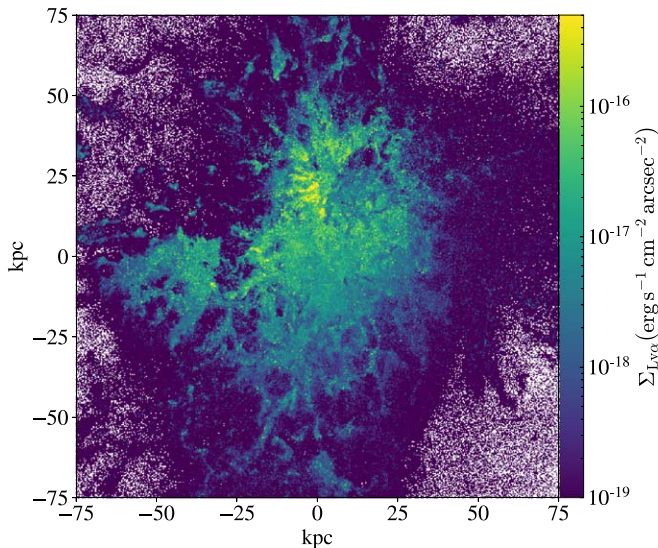


Figure 14. Example of a surface brightness image of an LAB where the luminosity is concentrated, which indicates the presence of an AGN, but the luminosity is not in a connected region.

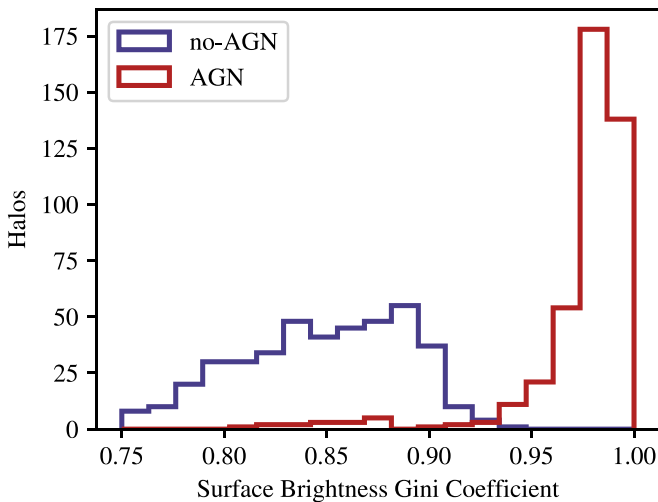


Figure 15. In our surface brightness images with an AGN, the escaping luminosity is much more spatially concentrated. We quantify this trend by computing the Gini coefficient for each snapshot we have, with and without an AGN, after convolving to the resolution of MUSE. By selecting a Gini coefficient threshold of around 0.93, one could reliably distinguish between blobs that contain and do not contain an AGN in our simulations.

ionized it provides a pathway along which Ly α is likely to escape; it is these pathways that produce the small region(s) of very intense surface brightness. However, the presence of a low-opacity pathway out of the blob decreases the probability that a photon will be scattered out into the extended blob structure before it escapes.

The presence of these small pathways out of the blob may be useful to detect the presence of an AGN in a blob (we include a visual demonstration of this phenomenon in Figure 14). We quantify the concentration of light of each blob by computing the Gini coefficient of a surface brightness image defined by

$$G = \frac{2 \sum_{i=1}^n i p_i}{n \sum_{i=1}^n p_i} - \frac{n+1}{n}, \quad (4)$$

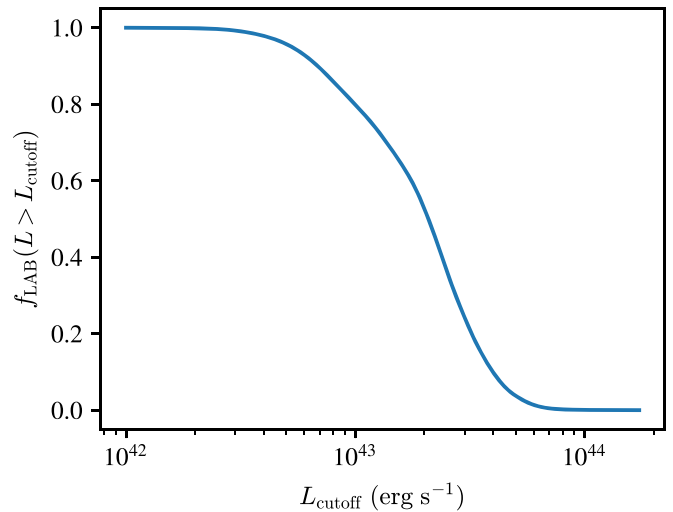


Figure 16. We use this distribution of the fraction of objects considered an LAB as a function of a luminosity cutoff to motivate and visualize the luminosity cutoffs presented in Figure 17. Our 100th, 75th, 50th, and 25th percentiles are 1.72×10^{44} , 2.96×10^{43} , 2.08×10^{43} , and 1.18×10^{43} , respectively.

where n is the number of pixels and the pixel luminosity data $p_1 \dots p_n$ are ordered by non-decreasing pixel brightness. We present histograms of the Gini coefficients for our model blobs with and without an AGN in Figure 15. For intuition, the Gini coefficient is always in the range $G \in [0, 1]$, corresponding to a range of scenarios bracketed by a uniform image ($G = 0$) to a single bright pixel ($G = 1$). The primary signature of the AGN's effect is to cause the luminosity to be concentrated in a much smaller area. While this may seem contradictory to the increase in total luminosity and area enclosed, note that this is a *relative* concentration. That is, while the diffuse emission is still significant, the central emission in the ionized bubble surrounding the AGN dominates when compared to this diffuse halo emission such that the overall concentration increases dramatically for the AGN-on model. This metric becomes more effective for identifying an AGN with higher resolution observations (Figure 5) since the bright patches of our surface brightness images are significantly smaller than the spatial resolution of current telescopes, but current technologies should be sufficient.

We do *not* propose that a Gini coefficient of specifically 0.93 will distinguish between observations of LABs that contain an AGN and those that do not. This metric is intended to demonstrate that it may be possible to distinguish between LABs that contain an AGN and those that do not from surface brightness features alone, and that the Gini coefficient may be an effective metric.

6. Physical Properties of LABs

We have thus far investigated the origin of Ly α photons in massive galaxies at high redshift, and demonstrated that they exhibit luminosities and spatial extents consistent with observed systems. We now turn our attention to the broader physical properties of the central galaxies and their parent halos of LABs. To do this, we adopt a fiducial luminosity cutoff of $L_{\text{Ly}\alpha} \geq 10^{43} \text{ erg s}^{-1}$ as an LAB. We do not include an AGN for any of the models presented here, so our results should be considered as representing no-AGN samples.

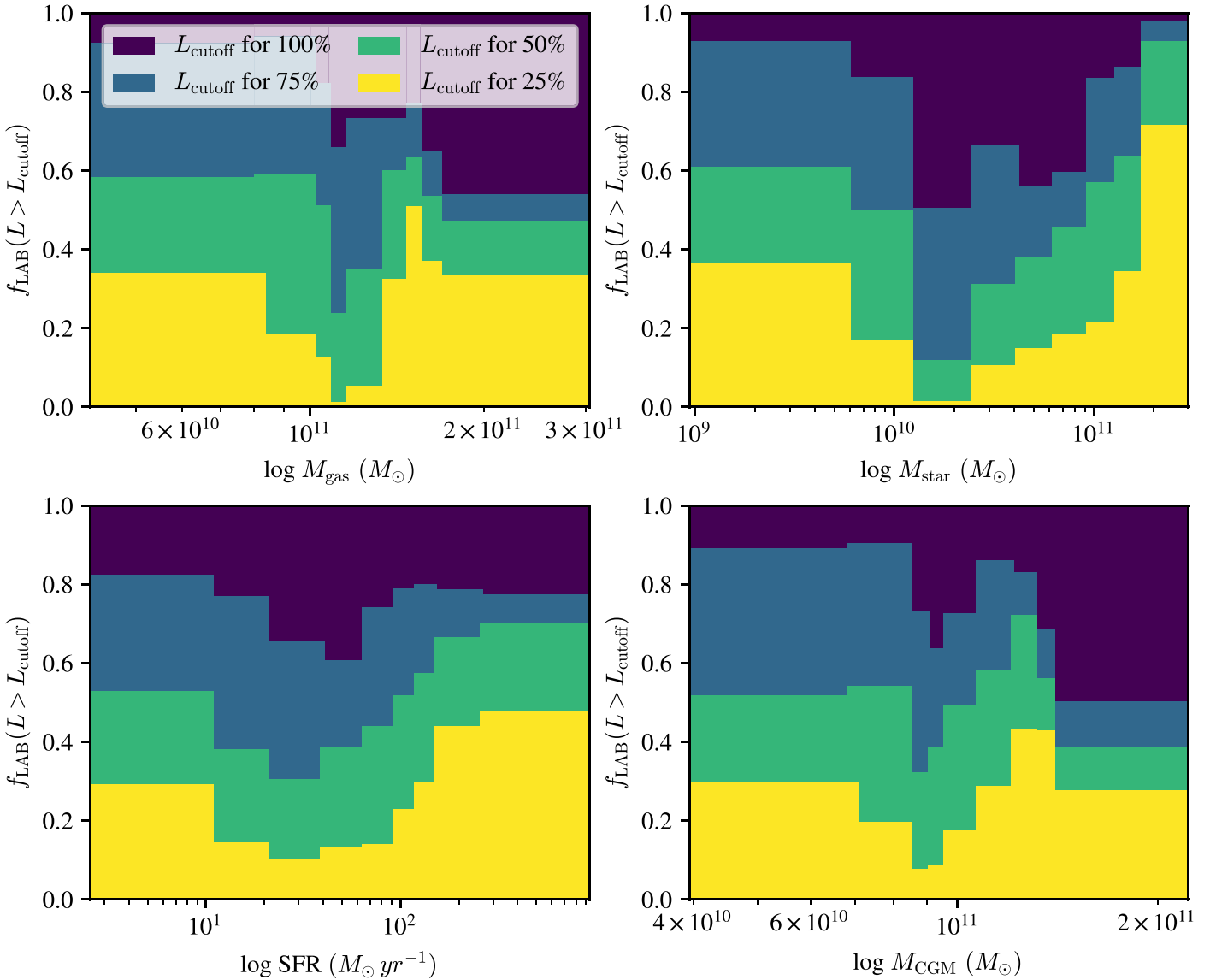


Figure 17. The cumulative fraction of halos in each bin that qualify as LABs according to different luminosity thresholds corresponding to quartiles of the overall sample, derived from the threshold distribution in Figure 16. This figure compares the distribution of LAB-hosting halos at specific luminosity cutoffs to demonstrate the relationship between the presence of an LAB and various physical properties, including the gas mass M_{gas} , stellar mass M_{star} , SFR, and CGM gas mass M_{CGM} . We see a weak trend in most of the properties, but stellar mass is the strongest predictor of LAB presence.

6.1. General Physical Properties and Thresholds

The first question we investigate is whether a single physical property defines when a galaxy becomes an LAB. In Figure 16, we show the cumulative fraction of halos that qualify as LABs according to a luminosity threshold, i.e., $f_{\text{LAB}} = N(L_{\text{Ly}\alpha} > L_{\text{cutoff}})/N$. Then in Figure 17, we show histograms of the gas mass, stellar mass, SFR, and CGM gas mass of the simulated galaxy at all times our simulations cover, by dividing all our snapshots along luminosity divisions that equally divide the population. The upper limits of these groups are 1.72×10^{44} , 2.96×10^{43} , 2.08×10^{43} , and 1.18×10^{43} . We use a particular definition for the CGM gas in this work: all gas contained within our simulation box (which is approximately $4 R_{\text{vir}}$ on a side) that is not part of the central massive galaxy, according to an FoF group finder with a linking length set to 0.2 times the mean interparticle separation. Each panel of this plot contains four histograms of the halo properties selected

based on luminosity thresholds that select 100%, 75%, 50%, and 25% of the total population. On the vertical axis is the fraction of halos in the range that meet that luminosity criteria. The general intention of this plot is to show (going from purple to yellow) how adding a more stringent luminosity cutoff alters the distribution of physical properties required to satisfy the cutoff.

In short, there are no sharp thresholds in physical properties within our modeled mass range, but we do see a general upwards trend toward greater LAB abundance with each of these physical properties, especially with M_* and SFR. But this trend is only strongly apparent at our most stringent luminosity threshold, $f_{\text{LAB}} = 0.25$, where the cutoff is at $L_{\text{Ly}\alpha} = 3.1 \times 10^{43} \text{ erg s}^{-1}$, likely signifying a “bigger things are bigger” effect.

What is more interesting is that the gas mass and CGM gas mass are very poor predictors of whether a halo meets a luminosity cutoff. At the outset, this may seem surprising. Indeed in Section 4.1, we discussed the origin of Ly α photons

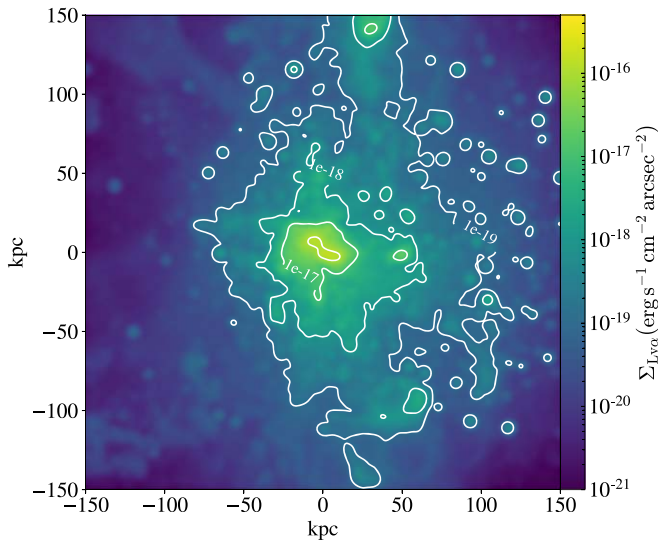


Figure 18. The Ly α surface brightness contours are at 10^{-16} , 10^{-17} , 10^{-18} , and 10^{-19} $\text{erg s}^{-1} \text{cm}^{-2} \text{arcsec}^{-2}$. Note that though this simulation domain is much larger than those we have discussed previously, it still does not encompass the full extent of a 10^{-19} contour. If one were to observe LABs with such sensitivity, one may find them much more extensive than previously published.

in the context of gas temperature and ionization state, both properties that likely correlate with the gas mass in a halo. That said, the physical concepts outlined in Section 4.1 describe the *production* of Ly α photons. While important, additionally critical for the observability of Ly α from galaxies is the *escape fraction*. As we demonstrated in Figure 10, there is a strong variation in the escape fraction of Ly α photons with viewing angle. While the production of Ly α is a straightforward function of the physical properties of the gas in the simulation, the escape fractions are significantly more complex.

The escape fraction from a massive halo depends on the covering fraction of neutral hydrogen and dust. Resonant scattering can either enhance the escape fraction by redirecting Ly α away from and around dusty media, or it can reduce the escape fraction by lengthening the path to escape, which increases the absorptive optical depth. The worst case for escape is when the emission is deeply embedded in an envelope of multiphase, dusty, neutral gas, such as young star-forming regions. This complexity, in essence, is what drives many of the computational challenges of these 3D Ly α radiative transport calculations.

6.2. Spatial Extent of Model LABs

We have already discussed the spatial extents of our model LABs in general, as well as in the context of observations in Figure 4. Here, we simply aggregate these findings for completeness when discussing the physical properties of blobs.

The size scales of observed LABs have no strict definition, and indeed their highly irregular morphologies makes deriving a simple radius nearly impossible. Instead, we advocate defining the size as the on-sky area within particular surface brightness contours. In Figure 4, we demonstrated that the areas of blobs both grow with time, i.e., at later times, the enclosed areas are generally larger. This is likely due to the increased availability of scattering gas, possibly as well as the growth of the SFR with time in massive halos. The sizes of these blobs increase with decreasing surface brightness cutoffs. We show

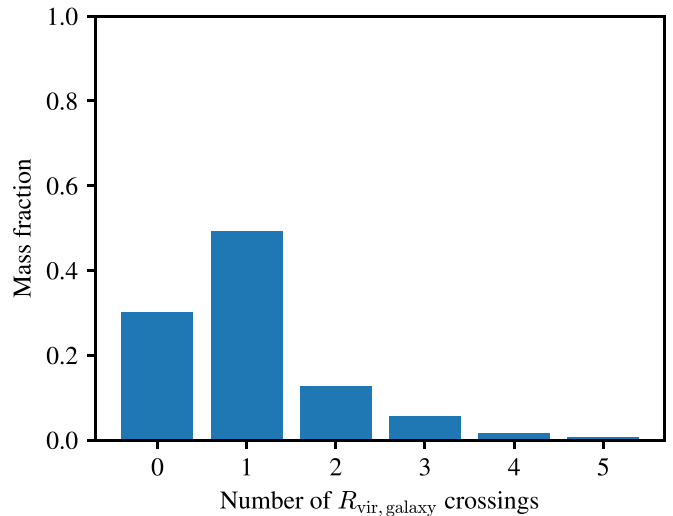


Figure 19. The fraction of gas that is part of the $z = 2$ halo but not the $z = 2$ central galaxy, broken up by the number of times the gas crosses the $z = 2$ central galaxy’s virial radius between $z = 2$ and $z = 5$.

this both in Figure 4, as well as in Figure 18, where we compute surface brightness contours for halo A4 down to a limiting surface brightness of 10^{-19} $\text{erg s}^{-1} \text{cm}^{-2} \text{arcsec}^{-2}$.

6.3. On the Origin of the Scattering Gas

We now turn our attention to the physical origin of the scattering gas that drives the large-scale spatial extents of LABs in our simulations. Specifically, is the scattering gas pristine gas newly infalling into the halo, or has it been recycled through the central galaxy at some point? To answer this, we examine our fiducial LAB at $z = 2$, and track the number of times that a given gas particle in the CGM (defined in Section 6) of this galaxy has crossed the central galaxy’s virial radius. We therefore do not distinguish in this case between diffuse CGM and gas associated with subhalos inside the main halo. To grasp an idea of the historical dynamics of the gas, we track the number of times each CGM particle crosses the central galaxy’s virial radius. In Figure 19, we show the mass fraction of particles as a function of the number of central galaxy R_{vir} crossings.

The majority of the scattering gas in this example LAB has crossed the virial radius at least once: only $\sim 30\%$ of the gas is pristine, while approximately 50% has passed through the central only once. While it is difficult to ascertain if the gas that has crossed the virial radius was ejected in a bona fide outflow (compared to, e.g., either never having been dynamically bound, or simply being at the edge of the friends of friends galaxy finder between snapshots), the relatively large fraction ($\sim 70\%$) of gas that has crossed the virial radius (and therefore been a member of the central galaxy) at some earlier time suggests that the overall baryon cycle between the central galaxy and CGM is important in driving the formation of high-redshift LABs.

7. Discussion

7.1. Uncertainties in the Model

In our modeling methods, we have made a number of assumptions that could potentially impact our results. Here, we explore these in turn.

7.1.1. Impact of the UV Background

LABs are noted for their spatial extent and one possible explanation for this extent is concentrated emission in dense regions which is scattered through an optically thick medium and thus dispersed across a wide structure. By contrast, it is possible that the spatial extent of a blob may be due to extended emission; namely, the outer regions of a gaseous halo that have been ionized, most likely by the cosmological UV background.

To test the impact of our assumed Faucher-Giguère et al. (2009) UV background we conduct a few experiments. First, we run COLT with the ionization state of the gas computed without the presence of any UV background. We find this has no effect on the observable luminosity of the blob, but this effect could be interpreted as evidence that the UV background is unimportant, or that the primary effect of the UV background is the photoheating effect that is included in the simulations, which we cannot remove. Therefore, we concentrate the remainder of our efforts on examining the effect of extremely intense UV backgrounds.

In Figure 9, we increase the UVB to $1.2 \times 10^{-17} \text{ erg cm}^{-2} \text{ s}^{-1} \text{ Hz}^{-1}$, which is a factor of 10^5 greater than the fiducial value from Faucher-Giguère et al. (2009) (small enhancements produce no visible effect at all). At this very elevated background, we see an erosion of the blob due to a reduced optical depth to scattering to Ly α photons in the CGM. The surface brightness image produced with the enhanced UV background level is both more compact and brighter; it is less like a blob. Specifically, the area of the LAB at a surface brightness level of $10^{-18} \text{ erg s}^{-1} \text{ cm}^{-2} \text{ arcsec}^{-2}$ at $z = 2$ decreases from 83–53 arcsec 2 . This argues against any substantial contribution from the UV background, and suggests that LABs are extended not because the source of their emission is itself extended, but because the Ly α emissions is scattered by the CGM.

7.1.2. Impact of IGM Transmissivity

In all previous sections we have neglected the effect of IGM extinction. In this section, we use the frequency-dependent IGM extinction data from Laursen et al. (2011) to compute an IGM transmission fraction for each snapshot based on its escaping spectrum, and plot these in Figure 20. While the IGM extinction can be substantial, it rarely alters the classification as an LAB.

7.1.3. Problems with the Hydro Simulations

We want to point out some specific flaws in the hydro simulations this work is based on that could be improved, and may have an impact on the results presented here.

The UVB photoheating that is used on-the-fly ignores self-shielding. While we are able to recompute the ionization state in post-processing, we cannot back out the temperature increase caused by the lack of self-shielding and then do ionizing radiative transfer more accurately.

While these simulations are zoom-in simulations, they almost certainly still suffer from significant resolution issues. With a higher resolution simulation we should be able to resolve more structure in the CGM and resolve the so-called multiphase CGM.

These simulations are also missing AGN feedback entirely. In this work we have demonstrated that the presence of an AGN has a large impact on the Ly α properties of LABs, so it is

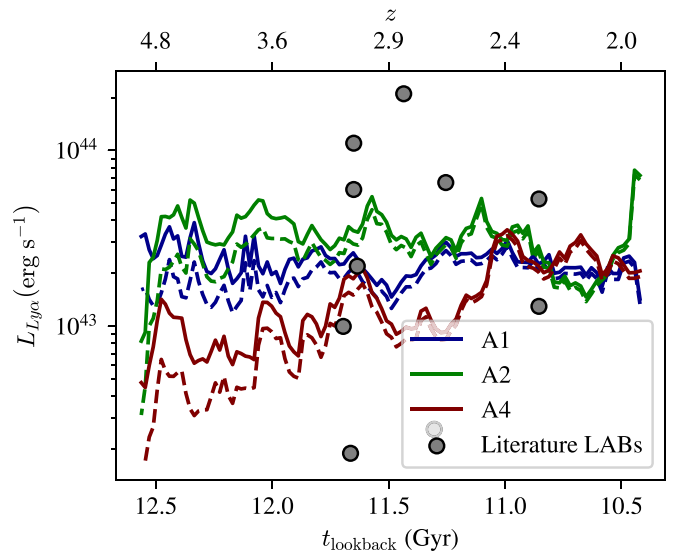


Figure 20. Ly α luminosity for a median line of sight for each galaxy in our sample (lines), with observational data from Table 1 overlotted as points, and curves for our sample, which include IGM extinction in dashed lines.

very likely that the thermal feedback, kinematics, and impact on star formation produced by an AGN are relevant too.

7.2. Comparison to Other Theories of LAB Formation

Our model includes the physics of emission from ionized gas surrounding star-forming regions, cooling from gas excited by collisions, and recombinations from ionized gas. As discussed in Section 5, we additionally (optionally) include the potential impact of an AGN on the Ly α luminosity from our model halos. This model builds on a rich history of literature models in this field that typically include only a subset of the aforementioned physics. In what follows, we discuss the findings of these models grouped by the physics they include.

Some of the previous work on LAB formation has been focused strongly on emission from cooling gas, that is, collisionally excited neutral hydrogen. Fardal et al. (2001) simulate only cooling emission and find luminosities of about the correct order of magnitude to be blobs, but would need to invoke yet-unquantified radiative transfer effects to explain the size. Haiman et al. (2000) found that cooling emission is sufficient to reproduce the blobs mentioned in Steidel et al. (2000) (but their model is a simple analytical one). Faucher-Giguère et al. (2010) also limited their model to cooling emission, but note that to reproduce the luminosities observed they needed to model cooling emission from regions that should be experiencing star formation. They did perform radiative transfer, and were able to reproduce the spatial extent of LABs and the characteristic line profile of Ly α nebulae. Rosdahl & Blaizot (2012) studied emission from cooling gas but additionally incorporated recombinations by treating them as a source of cooling, but were thus unable to discuss luminosity driven by recombinations.

In contrast to these works, Cantalupo et al. (2005) and Gronke & Bird (2017) omitted cooling emission from their model, but included emission from recombinations. We note that in our own model, for the non-AGN case, cooling emission dominates the Ly α luminosity. Kollmeier et al. (2010) modeled emission due to the cosmological UV background and the presence of a quasar (which they term fluorescence).

Some papers in the literature account for both emission from cooling and recombinations (Furlanetto et al. 2005; Cen & Zheng 2013; Geach et al. 2016; Smailagić et al. 2016). However, in all these papers the Ly α luminosity from recombinations is determined only by SFRs. An exception to this is the work of Geach et al. (2016), which accounts for the contribution of ionization from stars by locally modifying the ionization state of the gas based on the local SFR. In this work, we use stellar population synthesis on star particles from the simulations we are post-processing to compute an ionizing radiation field, and thus the ionization state of our gas. This different approach makes it possible to capture RT effects from the ionization state calculation as well.

Some of the previous attempts at LAB modeling do not include Ly α radiative transfer effects (Fardal et al. 2001; Furlanetto et al. 2005; Goerdt et al. 2010; Rosdahl & Blaizot 2012; Smailagić et al. 2016). For the existing work that does include RT, it is often restricted due to low spatial resolution (Cen & Zheng 2013) or discuss only a single line of sight (Cantalupo et al. 2005). In this paper we demonstrate that there are strong line-of-sight variations, which can only be reproduced with reasonably accurate RT calculations.

We now turn to whether other theoretical works for LAB formation agree with our own findings. Generally, all of the aforementioned studies that aim to model LABs find blob-like objects, but a few have notable results that are in agreement with our findings. Laursen & Sommer-Larsen (2007) found large surface brightness variation due to escape anisotropy in a simulated Lyman break galaxy. Cen & Zheng (2013) found ubiquitous blob-like objects around massive halos, as do we (albeit with a relatively small sample size). Kollmeier et al. (2010) reported cosmological-scale Ly α at a surface brightness of 10^{-19} erg s $^{-1}$ cm $^{-2}$ arcsec $^{-2}$, due to fluorescence. This result is quite similar to our own findings.

8. Conclusions

We have combined high-resolution cosmological zoom simulations of massive galaxy evolution at high redshift with 3D Monte Carlo Ly α radiative transfer simulations to develop a model for the origin of LABs at high redshift ($z = 2-5$). Our work considers the physics of ionization radiative transfer, cooling emission, recombination, and the impact of AGNs within the cosmological context of galaxy evolution. Our main conclusions from this work are as follows:

1. When adopting a notional luminosity-based definition for LAB formation, we find that all of our model massive galaxies go through an LAB phase at some point between $z = 2-5$ (see Figures 2, 3, 5, and 10). These LABs have extended morphologies in agreement with the observations.
2. The escape fraction of Ly α photons from these objects are highly orientation dependent, which complicates our observational understanding of the connection between LABs and massive galaxy evolution. Variations in the escape fraction with respect to different lines of sight can produce large variations in the observed Ly α luminosity (see Figure 13).
3. The formation of LABs in our model is independent of the inclusion of an AGN: star formation alone is enough to drive LAB formation in massive galaxies. That said, the presence of an AGN can significantly enhance Ly α

luminosities and alter the spatial extent (see Figures 4 and 10).

4. The presence of an AGN in an LAB may be detectable by measuring the spatial concentration of Ly α luminosity (see Figures 4 and 15).
5. The observed LAB luminosities do not scale very strongly with any individual physical property except for stellar mass. The reason is that the intrinsic luminosity is dependent on the temperature and ionization state of the gas, which can vary strongly with the small-scale geometry of the gas distribution. Similarly, the observed luminosity folds in the escape fraction, which is a strong function of the star-gas-dust geometry, as well as the small-scale clumping (see Figure 11).

Future improvements in the model could include both a full radiative hydrodynamic treatment of the galaxy formation simulations, as well as bona fide AGN feedback. Similarly, future generations of models that include lower mass halos may be able to connect LABs, LAEs, and Ly α halos.

We thank the referee for constructive comments and suggestions that have improved the quality of this work. We thank Claude-André Faucher-Giguère, Lluís Mas-Ribas, and George Privon for helpful conversations. D.N. acknowledges support from NSF-1909153. A.S. acknowledges support from program number HST-HF2-51421.001-A provided by NASA through a grant from the Space Telescope Science Institute, which is operated by the Association of Universities for Research in Astronomy, Incorporated, under NASA contract NAS5-26555. R.F. acknowledges financial support from the Swiss National Science Foundation (grant No. 157591). The simulations were run using XSEDE (TG-AST160048), supported by NSF grant ACI-1053575, Northwestern University’s compute cluster “Quest,” and on the University of Florida HiPerGator computing cluster. The data used in this work were, in part, hosted on facilities supported by the Scientific Computing Core at the Flatiron Institute, a division of the Simons Foundation. This work was initiated or performed in part at the Aspen Center for Physics, which is supported by NSF grant PHY-1607611.

Appendix A

Impact of Temperature on Our Model Results

Since the gas in the snapshots we are processing is potentially overheated due to the crude model for self-shielding in the hydrodynamic simulations, we examine the impact of halving the gas temperature in Figure 21 before the ionization state calculation or Ly α radiative transfer. We find that the luminosity due to collisions is decreased by about a factor of 1.5. There are at least two factors at play here: the effect on the ionization state and the effect on the gas temperature relation shown in Figure 11. The decrease in ionization state results in a decrease in the availability of free electrons to collisionally excite neutral hydrogen. Additionally, the decreased ionization state (mostly) decreases the escape fraction, which overall decreases the luminosity of the blob. In the bottom panel of Figure 21 we can see that the impact on emission due to collisional excitations is much more substantial than the effect of the impact on recombinations, but that a factor of 2 change in temperature is not sufficient to invalidate any of the previous

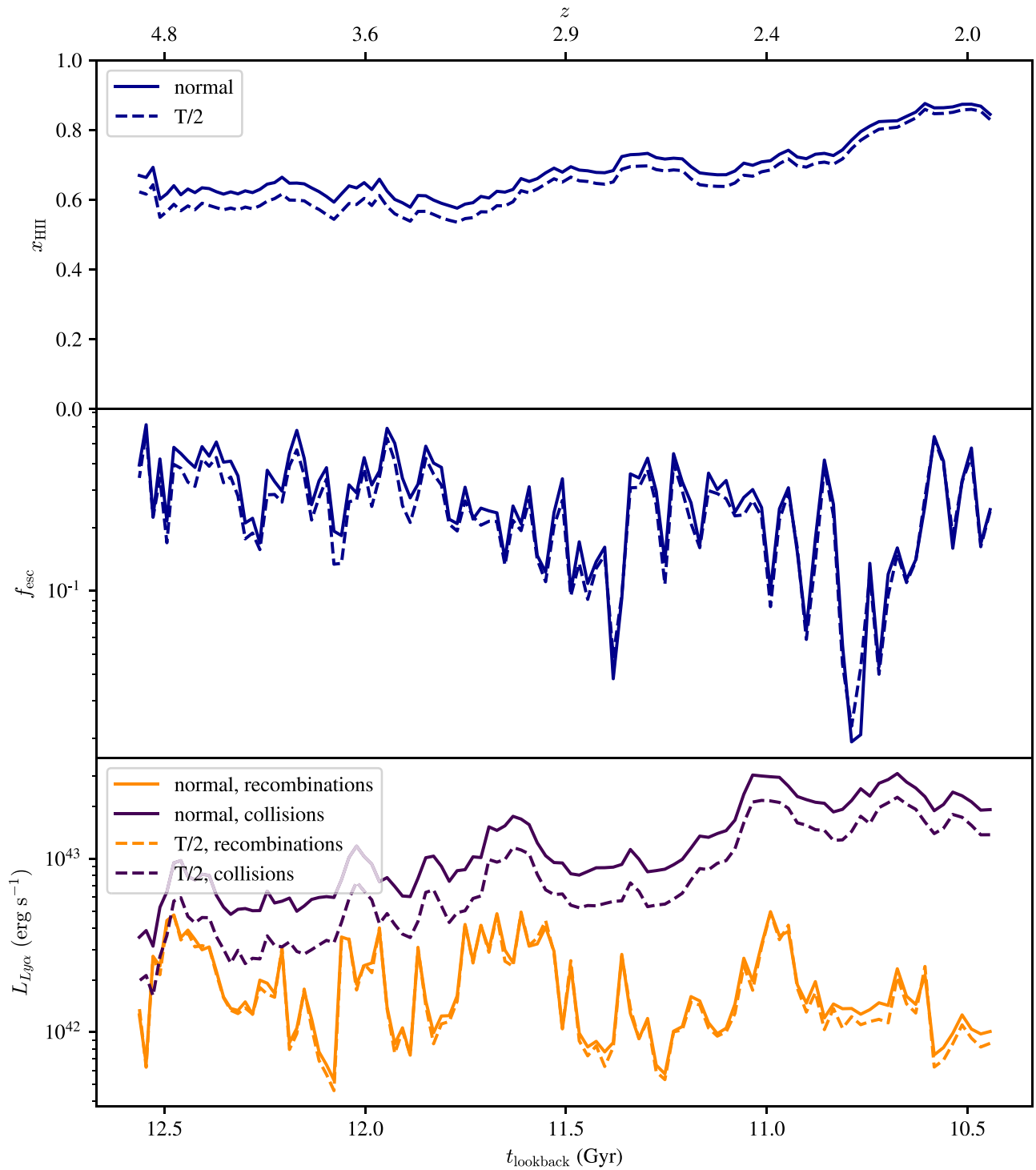


Figure 21. To assess the impact of the lack of the on-the-fly self-shielding approximation on the Ly α luminosity of our gas, we manually decrease the temperature of all gas in the simulation by a factor of 2, before computing the mass-weighted ionization fraction and performing Ly α radiative transfer calculations. The collisional excitation luminosity of our fiducial blob is slightly decreased.

conclusions in this work. That is, emission due to collisions dominate, and this has a luminosity typical of LABs.

Appendix B Physical Origin of Escaping Ly α

In Section 4.2 we noted that there are no strong trends between halo physical properties and whether emission from

recombinations or emission from collisional excitations dominate, and here we include Figure 22 to illustrate that explicitly.

As we have discussed previously in this work, the *escaping* Ly α luminosity, and variations in this escape fraction can be sufficient to confound simplistic reasoning about the powering source of blobs. Increasing the intrinsic emission of Ly α is not sufficient to drive observed (that is, escaping) luminosity of the

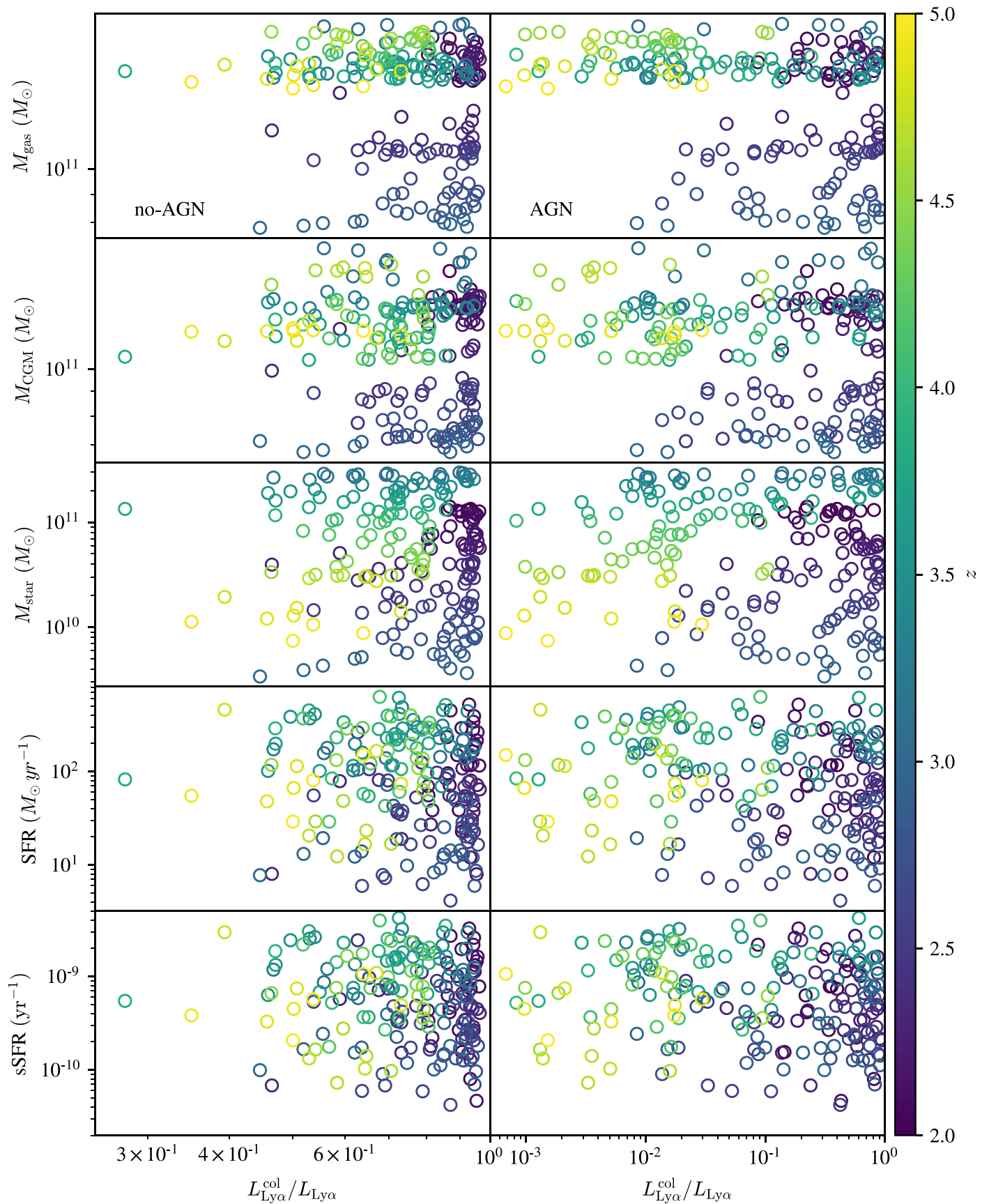


Figure 22. We plot the fraction of Ly α emission due to collisionally excited hydrogen as a function of various physical properties of the galaxy that one might expect to predict which source dominates the luminosity. The left column is for the mode where we do not account for the AGN, and on the right we account for ionization due to the AGN. Note the difference in the horizontal axis limits.






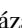





halo if the escape fraction of that increased luminosity decreases or is stochastic. For example, a growing population of neutral hydrogen will augment the collisional component of Ly α , but with that increased emission comes more Ly α optical depth, and thus more potential for the emitted Ly α to be absorbed by dust, depending on the geometry of the system. Further complicating this issue of physical property correlations is that the escape fraction of emission from collisionally excited hydrogen and recombinations differ, often by more than a factor of 2.

Appendix C

Testing the Impact of Our Assumed Core-skipping Approximation

Throughout this work, we have implemented a core-skipping algorithm for efficiency purposes (it improves the runtime by approximately an order of magnitude). Core-skipping is an approximation wherein photon packets that are in the core of the Ly α line and also in a cell, which is optically thick along all lines of sight, have their frequency shifted farther from line center. Here, we run a single snapshot without core skipping to get a concrete idea of its effects on our results. In this test, we see that turning off the core-skipping results in a small increase in the median escape fraction of about 3%.

ORCID iDs

Benjamin Kimock  <https://orcid.org/0000-0002-3160-7679>
 Desika Narayanan  <https://orcid.org/0000-0002-7064-4309>
 Aaron Smith  <https://orcid.org/0000-0002-2838-9033>
 Xiangcheng Ma  <https://orcid.org/0000-0001-8091-2349>
 Robert Feldmann  <https://orcid.org/0000-0002-1109-1919>
 Daniel Anglés-Alcázar  <https://orcid.org/0000-0001-5769-4945>
 Volker Bromm  <https://orcid.org/0000-0003-0212-2979>
 Romeel Davé  <https://orcid.org/0000-0003-2842-9434>
 James E. Geach  <https://orcid.org/0000-0003-4964-4635>
 Philip Hopkins  <https://orcid.org/0000-0003-3729-1684>
 Dušan Kereš  <https://orcid.org/0000-0002-1666-7067>

References

Alexander, D. M., Simpson, J. M., Harrison, C. M., et al. 2016, *MNRAS*, **461**, 2944
 Anglés-Alcázar, D., Davé, R., Faucher-Giguère, C.-A., Özel, F., & Hopkins, P. F. 2017a, *MNRAS*, **464**, 2840
 Anglés-Alcázar, D., Faucher-Giguère, C.-A., Quataert, E., et al. 2017b, *MNRAS*, **472**, L109
 Ao, Y., Matsuda, Y., Beelen, A., et al. 2015, *A&A*, **581**, A132
 Ao, Y., Zheng, Z., Henkel, C., et al. 2020, *NatAs*, **4**, 670
 Bădescu, T., Yang, Y., Bertoldi, F., et al. 2017, *ApJ*, **845**, 172
 Barger, A. J., Cowie, L. L., & Wold, I. G. B. 2012, *ApJ*, **749**, 106
 Bryan, G. L., & Norman, M. L. 1997, arXiv:astro-ph/9710187
 Caminha, G. B., Karman, W., Rosati, P., et al. 2016, *A&A*, **595**, A100
 Cantalupo, S., Porciani, C., Lilly, S. J., & Miniati, F. 2005, *ApJ*, **628**, 61
 Cen, R., & Zheng, Z. 2013, *ApJ*, **775**, 112
 Chapman, S. C., Richards, E. A., Lewis, G. F., Wilson, G., & Barger, A. J. 2001, *ApJL*, **548**, L147
 Cochrane, R. K., Hayward, C. C., Anglés-Alcázar, D., et al. 2019, *MNRAS*, **488**, 1779
 Daddi, E., Valentino, F., Rich, R. M., et al. 2020, arXiv:2006.11089
 Dijkstra, M. 2014, *PASA*, **31**, e040
 Eldridge, J. J., Izzard, R. G., & Tout, C. A. 2008, *MNRAS*, **384**, 1109
 Fardal, M. A., Katz, N., Gardner, J. P., et al. 2001, *ApJ*, **562**, 605

Faucher-Giguère, C.-A., Kereš, D., Dijkstra, M., Hernquist, L., & Zaldarriaga, M. 2010, *ApJ*, **725**, 633
 Faucher-Giguère, C.-A., Lidz, A., Zaldarriaga, M., & Hernquist, L. 2009, *ApJ*, **703**, 1416
 Feldmann, R., Hopkins, P. F., Quataert, E., Faucher-Giguère, C.-A., & Kereš, D. 2016, *MNRAS*, **458**, L14
 Fumagalli, M., Prochaska, J. X., Kasen, D., et al. 2011, *MNRAS*, **418**, 1796
 Furlanetto, S. R., Schaye, J., Springel, V., & Hernquist, L. 2005, *ApJ*, **622**, 7
 Fynbo, J. U., Möller, P., & Warren, S. J. 1999, *MNRAS*, **305**, 849
 Geach, J. E., Alexander, D. M., Lehmer, B. D., et al. 2009, *ApJ*, **700**, 1
 Geach, J. E., Narayanan, D., Matsuda, Y., et al. 2016, *ApJ*, **832**, 37
 Goerdt, T., Dekel, A., Sternberg, A., et al. 2010, *MNRAS*, **407**, 613
 Gronke, M., & Bird, S. 2017, *ApJ*, **835**, 207
 Hahn, O., & Abel, T. 2011, *MNRAS*, **415**, 2101
 Haiman, Z., & Rees, M. J. 2001, *ApJ*, **556**, 87
 Haiman, Z., Spaans, M., & Quataert, E. 2000, *ApJL*, **537**, L5
 Herenz, E. C., Hayes, M., & Scarlata, C. 2020, *A&A*, **642**, A55
 Hine, N. K., Geach, J. E., Alexander, D. M., et al. 2016, *MNRAS*, **455**, 2363
 Hopkins, P. F. 2015, *MNRAS*, **450**, 53
 Hopkins, P. F., Kereš, D., Oñorbe, J., et al. 2014, *MNRAS*, **445**, 581
 Hopkins, P. F., Narayanan, D., & Murray, N. 2013, *MNRAS*, **432**, 2647
 Hopkins, P. F., Richards, G. T., & Hernquist, L. 2007, *ApJ*, **654**, 731
 Hopkins, P. F., Wetzel, A., Kereš, D., et al. 2018, *MNRAS*, **480**, 800
 Hui, L., & Gnedin, N. Y. 1997, *MNRAS*, **292**, 27
 Katz, N., Weinberg, D. H., Hernquist, L., & Miralda-Escudé, J. 1996, *ApJL*, **457**, L57
 Kim, E., Yang, Y., Zabludoff, A., et al. 2020, *ApJ*, **894**, 33
 Kollmeier, J. A., Zheng, Z., Davé, R., et al. 2010, *ApJ*, **708**, 1048
 Kubo, M., Uchimoto, Y. K., Yamada, T., et al. 2013, *ApJ*, **778**, 170
 Laursen, P., & Sommer-Larsen, J. 2007, *ApJL*, **657**, L69
 Laursen, P., Sommer-Larsen, J., & Andersen, A. C. 2009, *ApJ*, **704**, 1640
 Laursen, P., Sommer-Larsen, J., & Razoumov, A. O. 2011, *ApJ*, **728**, 52
 Ma, X., Kasen, D., Hopkins, P. F., et al. 2015, *MNRAS*, **453**, 960
 Ma, X., Quataert, E., Wetzel, A., et al. 2020, *MNRAS*, **498**, 2001
 Mandelker, N., van den Bosch, F. C., Nagai, D., et al. 2020, *MNRAS*, **498**, 2415
 Mas-Ribas, L., & Dijkstra, M. 2016, *ApJ*, **822**, 84
 Matsuda, Y., Iono, D., Ohta, K., et al. 2007, *ApJ*, **667**, 667
 Matsuda, Y., Nakamura, Y., Morimoto, N., et al. 2009, *MNRAS*, **400**, L66
 Matsuda, Y., Yamada, T., Hayashino, T., et al. 2004, *AJ*, **128**, 569
 Matsuda, Y., Yamada, T., Hayashino, T., et al. 2011, *MNRAS*, **410**, L13
 Miley, G., & De Breuck, C. 2008, *A&ARv*, **15**, 67
 Nilsson, K. K., Fynbo, J. P. U., Möller, P., Sommer-Larsen, J., & Ledoux, C. 2006, *A&A*, **452**, L23
 North, P. L., Marino, R. A., Gorgoni, C., et al. 2017, *A&A*, **604**, A23
 Ohyama, Y., Taniguchi, Y., Kawabata, K. S., et al. 2003, *ApJL*, **591**, L9
 Ouchi, M., Ono, Y., Egami, E., et al. 2009, *ApJ*, **696**, 1164
 Overzier, R. A., Nesvadba, N. P. H., Dijkstra, M., et al. 2013, *ApJ*, **771**, 89
 Pengelly, R. M. 1964, *MNRAS*, **127**, 145
 Prescott, M. K. M., Dey, A., & Jannuzi, B. T. 2009, *ApJ*, **702**, 554
 Prescott, M. K. M., Dey, A., & Jannuzi, B. T. 2013, *ApJ*, **762**, 38
 Prescott, M. K. M., Kashikawa, N., Dey, A., & Matsuda, Y. 2008, *ApJL*, **678**, L77
 Prescott, M. K. M., Momcheva, I., Brammer, G. B., Fynbo, J. P. U., & Möller, P. 2015, *ApJ*, **802**, 32
 Rosdahl, J., & Blaizot, J. 2012, *MNRAS*, **423**, 344
 Scarlata, C., Colbert, J., Teplitz, H. I., et al. 2009, *ApJ*, **706**, 1241
 Scholz, T. T., & Walters, H. R. J. 1991, *ApJ*, **380**, 302
 Shibuya, T., Ouchi, M., Konno, A., et al. 2018, *PASJ*, **70**, S14
 Smailagić, M., Micic, M., & Martinović, N. 2016, *MNRAS*, **459**, 84
 Smith, A. 2020, *NatAs*, **4**, 648
 Smith, A., Ma, X., Bromm, V., et al. 2019, *MNRAS*, **484**, 39
 Smith, A., Safranek-Shrader, C., Bromm, V., & Milosavljević, M. 2015, *MNRAS*, **449**, 4336
 Smith, D. J. B., & Jarvis, M. J. 2007, *MNRAS*, **378**, L49
 Steidel, C. C., Adelberger, K. L., Shapley, A. E., et al. 2000, *ApJ*, **532**, 170
 Steidel, C. C., Bogosavljević, M., Shapley, A. E., et al. 2011, *ApJ*, **736**, 160
 Trebitsch, M., Verhamme, A., Blaizot, J., & Rosdahl, J. 2016, *A&A*, **593**, A122
 van Ojik, R., Roettgering, H. J. A., Miley, G. K., & Hunstead, R. W. 1997, *A&A*, **317**, 358
 Webb, T. M. A., Yamada, T., Huang, J. S., et al. 2009, *ApJ*, **692**, 1561
 Weingartner, J. C., & Draine, B. T. 2001, *ApJ*, **548**, 296

Wellons, S., Faucher-Giguère, C.-A., Anglés-Alcázar, D., et al. 2020, *MNRAS*, 497, 4051
Wilman, R. J., Gerssen, J., Bower, R. G., et al. 2005, *Natur*, 436, 227
Wisotzki, L., Bacon, R., Brinchmann, J., et al. 2018, *Natur*, 562, 229

Yang, Y., Zabludoff, A., Jahnke, K., et al. 2011, *ApJ*, 735, 87
Yang, Y., Zabludoff, A., Jahnke, K., & Davé, R. 2014, *ApJ*, 793, 114
Yang, Y., Zabludoff, A., Tremonti, C., Eisenstein, D., & Davé, R. 2009, *ApJ*, 693, 1579